Robust Task-Space Quadratic Programming for Kinematic-Controlled Robots

Mohamed Djeha, Pierre Gergondet, Abderrahmane Kheddar

Robust Task-Space Quadratic Programming for Kinematic-Controlled Robots

Mohamed Djeha, Pierre Gergondet, and Abderrahmane Kheddar, *Fellow, IEEE*

***Abstract*—Task-space quadratic programming (QP) is an elegant approach for controlling robots subject to constraints. Yet, in the case of kinematic-controlled (i.e., high-gains position or velocity) robots, closed-loop QP control scheme can be prone to instability depending on how the gains related to the tasks or the constraints are chosen. In this paper, we address such instability shortcomings. First, we highlight the non-robustness of the closed-loop system against non-modeled dynamics, such as those relative to joint-dynamics, flexibilities, external perturbations, etc. Then, we propose a robust QP control formulation based on high-level integral feedback terms in the task-space including the constraints. The proposed method is formally proved to ensure closed-loop robust stability and is intended to be applied to any kinematic-controlled robots under practical assumptions. We assess our approach through experiments on a fixed-base robot performing stable fast motions, and a floating-base humanoid robot robustly reacting to perturbations to keep its balance.**

***Index Terms*—Robust task-space control, Set robust stability, Quadratic Programming control, Kinematic-controlled robots**

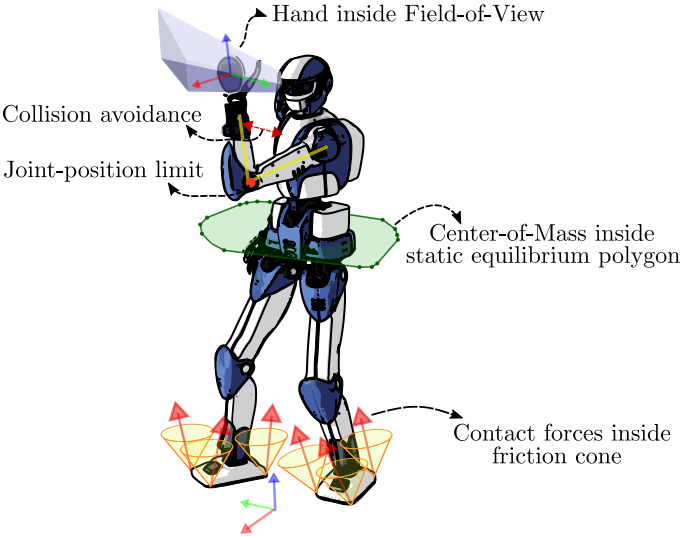

Fig. 1. Multi-objective control: HRP-4 robot right hand reaching a Cartesian target while being subject to several constraints.

I. Introduction

TASK-SPACE sensory control [1], [2] reached a high-level of maturity thanks to advances in numerical optimization methods. Non-linear task-space controllers can be formulated as local quadratic program (in short, QP control); which can handle several task-objectives and constraints using different sensors (embedded or external) for single or multiple different robots, see e.g., Fig. 1. QP controllers output desired joint torque $\boldsymbol{\tau}_{\mathrm{d}}$ and/or desired robot-state acceleration $\dot{\boldsymbol{\alpha}}_{\boldsymbol{q}_{\mathrm{d}}}$ that minimize at best (least-square sense) each task error, while ensuring that the robot state is within a set $\mathcal{C}$ of predefined constraints (also called *safety constraints* in control [3]). More particular to this work, we are interested in kinematic constraints (e.g., motion bounds in the joint or the task spaces, collision avoidance in the Cartesian space, field-of-view bounds in the image space, etc.) [4]; the task error is typically steered by a task-space PD controller [5].

QP control has been successfully applied to complex robots and use-cases [6]–[14]. Yet, several research reported sporadic unstable behaviors of relative severity (e.g., strong sustained oscillations), see e.g., [15]–[18]. These works used torque-controlled robots with *software-implemented* joint controllers (with the desired joint position and/or velocity as control input; see Fig. 2) that add a joint-feedback torque to increase the joint stiffness at the expense of pure torque-control compliance [19]. In particular, [15] noticed that oscillations and undesired behaviors are related to the double integration of the QP output $\dot{\boldsymbol{\alpha}}_{\boldsymbol{q}_{\mathrm{d}}}$. However, no further investigation was made to elucidate the cause. Instead, only workaround solutions have been proposed to mitigate the instability issue. These palliative methods can be sorted into two categories: (i) *low-level joint approaches* that prevent $\dot{\boldsymbol{\alpha}}_{\boldsymbol{q}_{\mathrm{d}}}$ double integration from diverging; typically by implementing a leaky integrator [20]; and (ii) *high-level approaches* where the QP formulation is substantially modified at the expense of a complex control-architecture [15], or by accounting for the joint feedback terms in the QP to adapt their gains [21] or for constraint feasibility concerns [22]. Other approaches reported that low-

Manuscript received May 17, 2022; revised February 14, 2023; accepted May 10, 2023. Date of publication Xxxxxxxx X, 20XX; date of current version Xxxxxxxxx X, 20XX. This paper was recommended for publication by Associate Editor Alexander Dietrich and Editor Paolo Robuffo Giordano upon evaluation of the reviewers comments. (*Corresponding author: Mohamed Djeha.*)

This work is supported in part by the Research Project I.AM. through the European Union H2020 program (GA 871899).

M. Djeha is with the École Militaire Polytechnique (EMP), Bordj El-Bahri, Algiers, Algeria. mohamed.djeha@lirmm.fr

A. Kheddar and P. Gergondet are with the CNRS-AIST Joint Robotics Laboratory, IRL, Tsukuba, Japan. pierre.gergondet@gmail.com

A. Kheddar is also with the CNRS-University of Montpellier LIRMM, Montpellier, France. kheddar@lirmm.fr

This paper has supplementary video downloadable material available at http://ieeexplore.ieee.org.

Color versions of one or more of the figures in this paper are available online at http://ieeexplore.ieee.org.

Digital Object Identifier 00.0000/XXX.202X.0000000

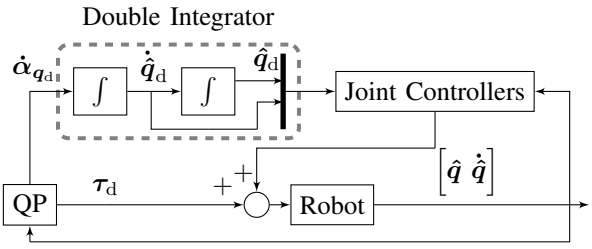

Fig. 2. QP control for torque-controlled robot with additional joint feedback.

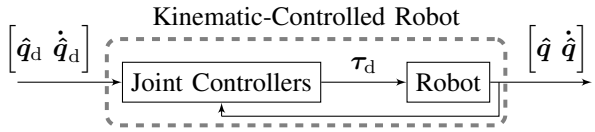

Fig. 3. Illustrative scheme of a kinematic-controlled robot. The difference between kinematic- and torque-controlled robots lies in how the joint controllers are implemented. In the former, they are strictly built-in by the manufacturer, whereas they can be software implemented or already built-in and proposed by the manufacturer as an additional joint-level control option.

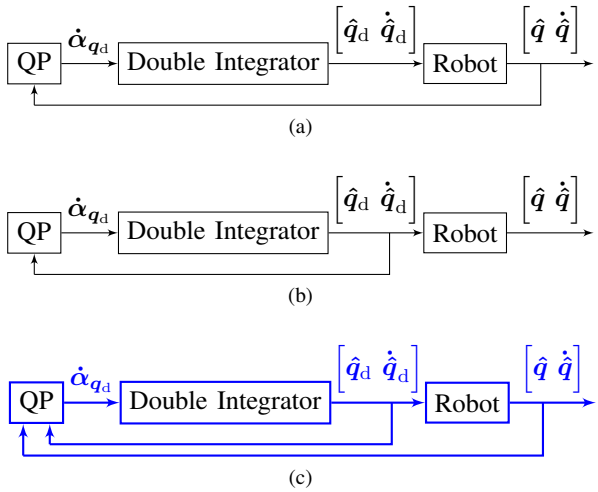

Fig. 4. Different closed-loop QP control schemes for kinematic-controlled robots. The 'Double integrator' and 'Robot' blocks are detailed in Fig. 2 and Fig. 3, respectively. (a) Feedback QP. (b) Feedforward QP. (c) Proposed robust QP. A detailed overview is shown in Fig. 5.

ering the task gains helps mitigate the instability [16], [18]. This induces that task gains are also an interfering factor. Similar observation is made in [5], [23], [24] concerning the gains of the constraint formulation. Unfortunately, since the joint controllers are software-implemented, their model and parameters are known.

Conversely, stiff kinematic-controlled robots[1] are torque-controlled robots with high-gains *hardware-implemented* joint controllers (Fig. 3). In this work, we are interested in high-stiffness joint controllers with desired joint position $\hat{\boldsymbol{q}}_\mathrm{d}$ or velocity $\dot{\hat{\boldsymbol{q}}}_\mathrm{d}$ as input. This control scheme is widely implemented in robotics and automation industry as it does not require knowledge of the robot's dynamics [28]–[35].

The closed-loop task-space QP controller combined with a kinematic-controlled robot, Fig. 4(a), is also prone to instability. This is because the joint-level controllers are not considered at the QP controller level. Such instability has been unnoticed in some control implementations that operate in feedforward (Fig. 4(b)). This leads to a decoupled control (similar to the approach adopted in [15]), delegating the control accuracy to the joint controllers [30], [36], [37]. Even though the latter have generally high gains to keep the joint tracking error as small as possible, the user has no guarantee on the accuracy of the performed motion[2]. In such cases, frequent initializations of the controller are needed (i.e., start a new instance of the QP control with an update of the model at task switching, or integrator memory reset), to lower the discrepancy between real and control-model states due to non-modeled flexibilities or external disturbances.

In this paper, we address the stability of closed-loop task-space QP control (Section II) in the context of kinematic-controlled robots. We show in Section III how the closed-loop instability is interpreted in terms of non-robustness of the QP feedback scheme (Fig. 4(a)) against non-modeled joint-dynamics[3], flexibilities, external disturbances, etc. We propose a robust feedback QP control formulation (Fig. 4(c)) based on high-level integral feedback terms that robustify the task-space PD controller (task robust stability) and the constraint formulation (set robust stability), see Fig. 5. We extend its implementation to weighted-prioritized multi-objective QP control in Section IV. We assess our controller with experiments on two robots: (i) a fixed-base robot Panda performing highly-dynamic motion control, and (ii) floating-based humanoid robot HRP-4 performing robust balance control under non-modeled flexibilities and external disturbances (Section V).

The stability analysis, based on Lyapunov theory, focuses on intrinsic closed-loop QP control (i.e., not considering other sources or nature of instability such as singularities for which we dedicated a specific analysis in [39] or discretization). Our solution is elegant as it applies directly to the existing QP-templated tasks. In contrast to [23] where the joint controllers model is required, our approach is straightforwardly used with any kinematic-controlled robot as it does not require the exact knowledge of the joint-dynamics model which we only assume to be Input-to-State-Stable (ISS). We also further advanced [36] in two ways: (i) we account for the lack of joint-dynamics in closed-loop; (ii) we include the constraints in the stability analysis. Although we define the set robust stability similarly to [40], our approach is different in three main points: (i) the factors against which the robustness is enforced, (ii) the formalism adopted to prove robustness, and (iii) the nature of the term added to achieve robustness.

To sum-up, our contributions are as follows:

- Robust task formulation;
- Robust constraint formulation;

[1]In literature, they are referred to in different ways: position-controlled robots, velocity-controlled robots, low-level impedance-controlled robots [25], [26] and stiffness-controlled robots [27].

[2]https://youtu.be/gTVi1QsLQU4

[3]The parameters of the joint-dynamics (joint controllers + actuators) are generally not known as they depend on the joint controller gains (fixed by the manufacturer not intended to be modified by the operator in almost all robots [38]) and the actuators electro-mechanical constants.

- Task stability investigations in the case of multi-objective weighted-prioritized robust constrained QP;
- Integration into our existing framework and validation on a robotic manipulator and a humanoid robot.

The notations and definitions used in this paper are described in Appendix A.

II. Task-Space QP Control Formulation

A. Joint-Dynamics

Consider a robot with a floating or a fixed base having $n \in \mathbb{N}$ actuated Degrees-of-Freedom (DoF). Its state is defined by

$$\begin{aligned} \boldsymbol{q}^\mathsf{T} &= \begin{bmatrix} \boldsymbol{\xi}^\mathsf{T} & \hat{\boldsymbol{q}}^\mathsf{T} \end{bmatrix} \in \mathbb{R}^{7+n} \\ \boldsymbol{\alpha}_{\boldsymbol{q}}^\mathsf{T} &= \begin{bmatrix} \boldsymbol{v}^\mathsf{T} & \dot{\hat{\boldsymbol{q}}}^\mathsf{T} \end{bmatrix} \in \mathbb{R}^{6+n} \\ \dot{\boldsymbol{\alpha}}_{\boldsymbol{q}}^\mathsf{T} &= \begin{bmatrix} \dot{\boldsymbol{v}}^\mathsf{T} & \ddot{\hat{\boldsymbol{q}}}^\mathsf{T} \end{bmatrix} \in \mathbb{R}^{6+n} \end{aligned}. \tag{1}$$

$\boldsymbol{\xi}^\mathsf{T} = \begin{bmatrix} \boldsymbol{p}^\mathsf{T} & \underline{\mathbf{q}}^\mathsf{T} \end{bmatrix} \in \mathbb{R}^7$ is the floating base position $\boldsymbol{p} \in \mathbb{R}^3$ and orientation parameterized with unit quaternion $\underline{\mathbf{q}} \in S^3$ (3-sphere), $\hat{\boldsymbol{q}} \in \mathbb{R}^n$ is the joint position. $\boldsymbol{v} \in \mathbb{R}^6$ (resp. $\dot{\boldsymbol{v}} \in \mathbb{R}^6$) is the linear and angular floating-base velocities (resp. floating-base accelerations), and $\dot{\hat{\boldsymbol{q}}} \in \mathbb{R}^n$ (resp. $\ddot{\hat{\boldsymbol{q}}} \in \mathbb{R}^n$) is the joint velocity (resp. joint acceleration). $\boldsymbol{q}_\mathrm{d}$, $\boldsymbol{\alpha}_{\boldsymbol{q}_\mathrm{d}}$ and $\dot{\boldsymbol{\alpha}}_{\boldsymbol{q}_\mathrm{d}}$ denote the desired $\boldsymbol{q}$, $\boldsymbol{\alpha}_{\boldsymbol{q}}$ and $\dot{\boldsymbol{\alpha}}_{\boldsymbol{q}}$ in (1), respectively.

The robot is governed by the equation of motion

$$\mathbf{M}(\boldsymbol{q})\dot{\boldsymbol{\alpha}}_{\boldsymbol{q}_\mathrm{d}} + \boldsymbol{h}(\boldsymbol{q}, \boldsymbol{\alpha}_{\boldsymbol{q}}) - \mathbf{J}^{\mathrm{c}\mathsf{T}}\boldsymbol{f} = \mathbf{S}_{\boldsymbol{\tau}}\boldsymbol{\tau}, \tag{2}$$

where $\mathbf{M}(\boldsymbol{q}) \in \mathbb{R}^{(6+n)\times(6+n)}$ is the inertia matrix, $\boldsymbol{h}(\boldsymbol{q}, \boldsymbol{\alpha}_{\boldsymbol{q}}) \in \mathbb{R}^{6+n}$ gathers Coriolis-centrifugal and gravitational torques, $\mathbf{J}^\mathrm{c} \in \mathbb{R}^{3\times(6+n)}$ is the contact Jacobian and $\boldsymbol{f} \in \mathbb{R}^3$ is the contact force. $\mathbf{S}_{\boldsymbol{\tau}}^\mathsf{T} = \begin{bmatrix} \mathbf{0}_{n\times 6} & \mathbf{I}_n \end{bmatrix} \in \mathbb{R}^{n\times(6+n)}$ is the actuation selection matrix, and $\boldsymbol{\tau} \in \mathbb{R}^n$ is the joint torque such that

$$\boldsymbol{\tau}_\mathrm{min} \leq \boldsymbol{\tau} \leq \boldsymbol{\tau}_\mathrm{max}, \tag{3}$$

where $\boldsymbol{\tau}_\mathrm{min}, \boldsymbol{\tau}_\mathrm{max} \in \mathbb{R}^n$ are the joint torque bounds. Constraints (2) and (3) can be combined resulting in the torque-bounded equations of motion

$$\mathbf{S}_{\boldsymbol{\tau}}\boldsymbol{\tau}_\mathrm{min} \leq \mathbf{M}(\boldsymbol{q})\dot{\boldsymbol{\alpha}}_{\boldsymbol{q}_\mathrm{d}} + \boldsymbol{h}(\boldsymbol{q}, \boldsymbol{\alpha}_{\boldsymbol{q}}) - \mathbf{J}^{\mathrm{c}\mathsf{T}}\boldsymbol{f} \leq \mathbf{S}_{\boldsymbol{\tau}}\boldsymbol{\tau}_\mathrm{max}. \tag{4}$$

The contact force is constrained to its linearized friction cone

$$\boldsymbol{f} = \sum_{j=1}^{n_c} \beta_j \boldsymbol{\rho}_j,\ \beta_j \geq 0,\ j = 1, \ldots, n_c, \tag{5}$$

where $\boldsymbol{\rho}_j \in \mathbb{R}^3$ is the j^th vector of the linearized friction cone, and $n_c > 2$ being the total number of the linearized friction-cones' vectors, see [41].

Let $\boldsymbol{x}, \boldsymbol{x}_\mathrm{d} \in \mathbb{R}^{13+2n}$ defined as

$$\boldsymbol{x}^\mathsf{T} = \begin{bmatrix} \boldsymbol{q}^\mathsf{T} & \boldsymbol{\alpha}_{\boldsymbol{q}}^\mathsf{T} \end{bmatrix},\ \boldsymbol{x}_\mathrm{d}^\mathsf{T} = \begin{bmatrix} \boldsymbol{q}_\mathrm{d}^\mathsf{T} & \boldsymbol{\alpha}_{\boldsymbol{q}_\mathrm{d}}^\mathsf{T} \end{bmatrix}, \tag{6}$$

be the actual and desired robot states, respectively. In particular, $\boldsymbol{x}_\mathrm{d}$ follows a double integrator dynamics (in the continuous time-domain)

$$\boldsymbol{\alpha}_{\boldsymbol{x}_\mathrm{d}} = \begin{bmatrix} \boldsymbol{\alpha}_{\boldsymbol{q}_\mathrm{d}} \\ \dot{\boldsymbol{\alpha}}_{\boldsymbol{q}_\mathrm{d}} \end{bmatrix} = \begin{bmatrix} \mathbf{0} & \mathbf{I}_{6+n} \\ \mathbf{0} & \mathbf{0} \end{bmatrix} \boldsymbol{x}_\mathrm{d} + \begin{bmatrix} \mathbf{0} \\ \mathbf{I}_{6+n} \end{bmatrix} \dot{\boldsymbol{\alpha}}_{\boldsymbol{q}_\mathrm{d}}, \tag{7}$$

with $\dot{\boldsymbol{\alpha}}_{\boldsymbol{q}_\mathrm{d}} \in \mathcal{U}$ where $\mathcal{U} \subseteq \mathbb{R}^{6+n}$ is the set of $\dot{\boldsymbol{\alpha}}_{\boldsymbol{q}_\mathrm{d}}$ admissible values. The actual floating-base state $\boldsymbol{x}^{\mathrm{FB}\mathsf{T}} = \begin{bmatrix} \boldsymbol{\xi}^\mathsf{T} & \boldsymbol{v}^\mathsf{T} \end{bmatrix} \in \mathbb{R}^{13}$ is assumed to be bounded and estimated by an observer. In particular, let us define the robot-state tracking error $\boldsymbol{\phi}$ as

$$\begin{aligned} \boldsymbol{\phi} &= \boldsymbol{x} - \boldsymbol{x}_\mathrm{d}, \\ &\stackrel{\mathrm{def}}{=} \begin{bmatrix} \boldsymbol{\xi} \ominus \boldsymbol{\xi}_\mathrm{d} \\ \hat{\boldsymbol{q}} - \hat{\boldsymbol{q}}_\mathrm{d} \\ \boldsymbol{v} - \boldsymbol{v}_\mathrm{d} \\ \dot{\hat{\boldsymbol{q}}} - \dot{\hat{\boldsymbol{q}}}_\mathrm{d} \end{bmatrix} \in \mathbb{R}^{13+2n}, \end{aligned} \tag{8}$$

where $\boldsymbol{\xi} \ominus \boldsymbol{\xi}_\mathrm{d} \stackrel{\mathrm{def}}{=} \begin{bmatrix} \boldsymbol{p} - \boldsymbol{p}_\mathrm{d} \\ \underline{\mathbf{q}} \otimes \underline{\mathbf{q}}_\mathrm{d}^{-1} \end{bmatrix} \in \mathbb{R}^7$ encompasses the position and orientation errors between $\boldsymbol{\xi}$ and $\boldsymbol{\xi}_\mathrm{d}$ where $\otimes$ denotes the quaternion product [42, Section 2.6].

Given a kinematic-controlled robot (Fig. 3), the actual robot state is governed by the dynamics of its actuated joints. By extracting the actuated joints parts from $\boldsymbol{x}$ and $\boldsymbol{x}_\mathrm{d}$ in (6), let $\hat{\boldsymbol{x}}_\mathrm{d}, \hat{\boldsymbol{x}} \in \mathbb{R}^{2n}$ defined as

$$\hat{\boldsymbol{x}}^\mathsf{T} = \begin{bmatrix} \hat{\boldsymbol{q}}^\mathsf{T} & \dot{\hat{\boldsymbol{q}}}^\mathsf{T} \end{bmatrix},\ \hat{\boldsymbol{x}}_\mathrm{d}^\mathsf{T} = \begin{bmatrix} \hat{\boldsymbol{q}}_\mathrm{d}^\mathsf{T} & \dot{\hat{\boldsymbol{q}}}_\mathrm{d}^\mathsf{T} \end{bmatrix}, \tag{9}$$

be the actual and desired states of the robot actuated DoF. Similarly, we define the joint-dynamics tracking error $\hat{\boldsymbol{\phi}}$ as

$$\hat{\boldsymbol{\phi}} = \hat{\boldsymbol{x}} - \hat{\boldsymbol{x}}_\mathrm{d} \in \mathbb{R}^{2n}, \tag{10}$$

and which dynamics[4] is

$$\dot{\hat{\boldsymbol{\phi}}} = \boldsymbol{f}_{\hat{\boldsymbol{\phi}}}(\hat{\boldsymbol{\phi}}, \boldsymbol{\tau}_\mathrm{l}), \tag{11}$$

where $\boldsymbol{\tau}_\mathrm{l} \in \mathbb{R}^n$ is the bounded joint-space disturbance torque input. In this study, we consider that $\boldsymbol{f}_{\hat{\boldsymbol{\phi}}}$ is not known exactly but its main property is given by the following assumption.

Assumption 1. *The joint-dynamics $\boldsymbol{f}_{\hat{\boldsymbol{\phi}}}$ in (11) is ISS w.r.t $\boldsymbol{\tau}_\mathrm{l}$. Namely, there exist a class $\mathcal{KL}$ function β and a class $\mathcal{K}$ function γ, such that for any initial state $\hat{\boldsymbol{\phi}}(0)$ and any bounded disturbance input $\boldsymbol{\tau}_\mathrm{l}(t)$, the solution $\hat{\boldsymbol{\phi}}(t)$ exists $\forall t \geq 0$ and satisfies [43], [44]*

$$\left\|\hat{\boldsymbol{\phi}}(t)\right\| \leq \beta\left(\left\|\hat{\boldsymbol{\phi}}(0)\right\|, t\right) + \gamma\left(\left\|\boldsymbol{\tau}_\mathrm{l}\right\|_\infty\right) \tag{12}$$

The IS-Stability ensures that, given bounded disturbance inputs $\boldsymbol{\tau}_\mathrm{l}$, the joint-dynamics tracking error $\hat{\boldsymbol{\phi}}$ in (10) evolves in a bounded set containing the origin. Assumption 1 is largely valid as it is among the main requirement for the well-functioning of a kinematic-controlled robot. $\boldsymbol{\phi}$ in (8) reflects the effect of several kinds of disturbances and uncertainties. Namely, non-modeled dynamics (e.g., transient joint-dynamics response w.r.t $\hat{\boldsymbol{x}}_\mathrm{d}$, flexibilities, etc.); hardware imperfections (e.g., joint-dynamics steady-state errors, etc.); external disturbance $\boldsymbol{\tau}_\mathrm{l} \neq 0$ (e.g., loads, pushes, unexpected impacts, etc.); measurement and estimation noises (joint-velocity and floating-base estimations, etc.); and possibly others[5].

Remark 1. *For a fixed-base robot, $\boldsymbol{q} = \hat{\boldsymbol{q}}$ and $\boldsymbol{\alpha}_{\boldsymbol{q}} = \dot{\hat{\boldsymbol{q}}}$ leading to $\boldsymbol{x} = \hat{\boldsymbol{x}}$ (respectively for the corresponding desired states), and $\boldsymbol{\phi} = \hat{\boldsymbol{\phi}}$.*

[4]For the sake of generality, both $\hat{\boldsymbol{q}}_\mathrm{d}$ or $\dot{\hat{\boldsymbol{q}}}_\mathrm{d}$ (joint commands) are encompassed by $\hat{\boldsymbol{x}}_\mathrm{d}$ in the joint-dynamics $\boldsymbol{f}_{\hat{\boldsymbol{\phi}}}$ in (11).

[5]A benchmark problem has been proposed in [45] to simulate such disturbances.

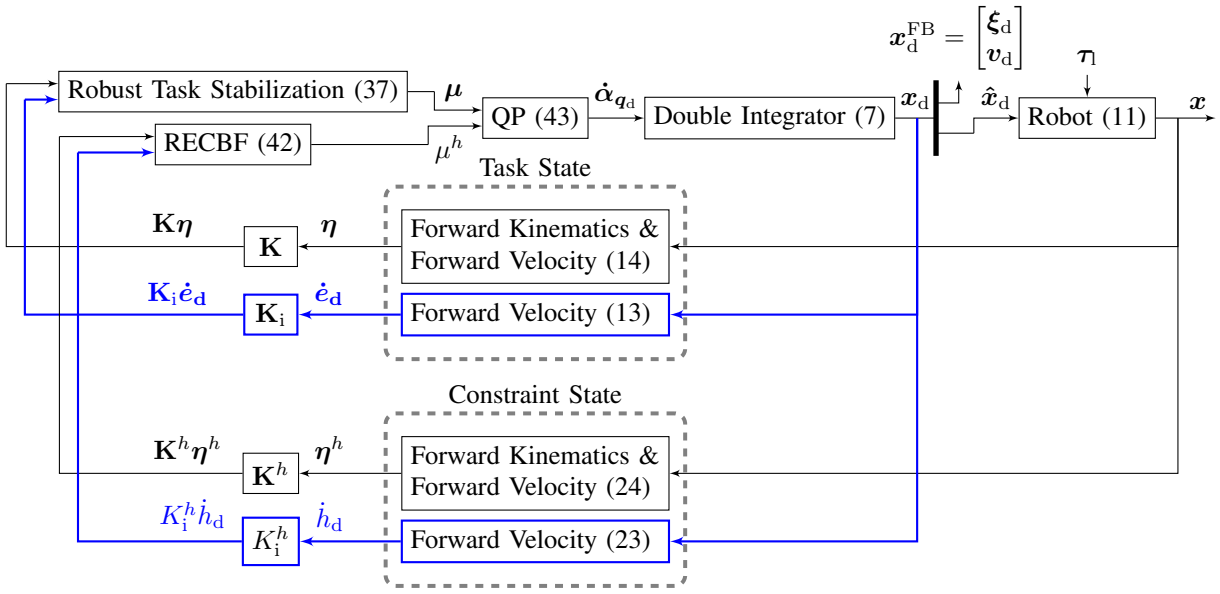

Fig. 5. Overview of the proposed robust QP control scheme. The blue thick paths show the high-level integral feedback. Note that if $\mathbf{K}_{\mathrm{i}} = \mathbf{0}$ and $K_{\mathrm{i}}^h = 0$, correspond to the feedback control scheme in Fig. 4a.

B. Input-Output Task Dynamics

Let $\boldsymbol{s}\colon \mathbb{R}^{7+n} \to \mathbb{R}^m$ be the forward kinematics for a given task defined by m coordinates, and $\boldsymbol{s}_{\mathrm{ref}}(t), \dot{\boldsymbol{s}}_{\mathrm{ref}}(t), \ddot{\boldsymbol{s}}_{\mathrm{ref}}(t) \in \mathbb{R}^m$ be the task references; we can define the following states

$$\boldsymbol{\eta}_{\mathrm{d}}(\boldsymbol{x}_{\mathrm{d}}) = \begin{bmatrix}\boldsymbol{e}_{\mathbf{d}} \\ \dot{\boldsymbol{e}}_{\mathbf{d}}\end{bmatrix} = \begin{bmatrix}\boldsymbol{s}(\boldsymbol{q}_{\mathrm{d}}) - \boldsymbol{s}_{\mathrm{ref}}(t) \\ \mathbf{J}_{\mathrm{d}}\boldsymbol{\alpha}_{\boldsymbol{q}_{\mathrm{d}}} - \dot{\boldsymbol{s}}_{\mathrm{ref}}(t)\end{bmatrix} \in H \subset \mathbb{R}^{2m}, \quad (13)$$

$$\boldsymbol{\eta}(\boldsymbol{x}) = \begin{bmatrix}\boldsymbol{e} \\ \dot{\boldsymbol{e}}\end{bmatrix} = \begin{bmatrix}\boldsymbol{s}(\boldsymbol{q}) - \boldsymbol{s}_{\mathrm{ref}}(t) \\ \mathbf{J}\boldsymbol{\alpha}_{\boldsymbol{q}} - \dot{\boldsymbol{s}}_{\mathrm{ref}}(t)\end{bmatrix} \in H \subset \mathbb{R}^{2m}, \quad (14)$$

where $\mathbf{J}_{\mathrm{d}}, \mathbf{J} \in \mathbb{R}^{m\times(6+n)}$ are the task Jacobians computed w.r.t $\boldsymbol{q}_{\mathrm{d}}$ and $\boldsymbol{q}$, respectively; $\boldsymbol{\eta}_{\mathrm{d}}(\boldsymbol{x}_{\mathrm{d}})$ and $\boldsymbol{\eta}(\boldsymbol{x})$ denote the desired and actual task dynamics states, respectively; H is the set of their admissible values.

Using Taylor expansion and (8), a relation between $\boldsymbol{\eta}$ and $\boldsymbol{\eta}_{\mathrm{d}}$ is obtained as

$$\begin{aligned}\boldsymbol{\eta}(\boldsymbol{x}) &= \boldsymbol{\eta}(\boldsymbol{x}_{\mathrm{d}} + \boldsymbol{\phi}), \\ &= \boldsymbol{\eta}(\boldsymbol{x})\big|_{\boldsymbol{x}=\boldsymbol{x}_{\mathrm{d}}} + \underbrace{\frac{\partial\boldsymbol{\eta}(\boldsymbol{x})}{\partial\boldsymbol{x}}\bigg|_{\boldsymbol{x}=\check{\boldsymbol{x}}}}_{\boldsymbol{\eta}_{\boldsymbol{\phi}}}\boldsymbol{\phi}, \ \check{\boldsymbol{x}} = \boldsymbol{x}_{\mathrm{d}} + \theta\boldsymbol{\phi}, \\ &= \boldsymbol{\eta}_{\mathrm{d}}(\boldsymbol{x}_{\mathrm{d}}) + \boldsymbol{\eta}_{\boldsymbol{\phi}}, \ \frac{\partial\boldsymbol{\eta}(\boldsymbol{x})}{\partial\boldsymbol{x}} = \begin{bmatrix}\mathbf{J} & \mathbf{0} \\ \frac{\partial(\mathbf{J}\boldsymbol{\alpha}_{\boldsymbol{q}})}{\boldsymbol{q}} & \mathbf{J}\end{bmatrix},\end{aligned} \quad (15)$$

$0 \leq \theta \leq 1$; $\boldsymbol{\eta}_{\boldsymbol{\phi}} \in \mathbb{R}^m$ being the Lagrange remainder of the Taylor expansion and denotes the mapping of $\boldsymbol{\phi}$ in task-space. Hereafter, the dependency of $\boldsymbol{\eta}_{\mathrm{d}}$ on $\boldsymbol{x}_{\mathrm{d}}$ and $\boldsymbol{\eta}$ on $\boldsymbol{x}$ is dropped.

Remark 2. *In the multiplication* $\frac{\partial\boldsymbol{\eta}(\boldsymbol{x})}{\partial\boldsymbol{x}}\Big|_{\boldsymbol{x}=\check{\boldsymbol{x}}}\boldsymbol{\phi}$*, only the vector part of* $\underline{\mathbf{q}} \otimes \underline{\mathbf{q}}_{\mathrm{d}}^{-1}$ *is considered in* $\boldsymbol{\phi}$ (8).

Given that $\boldsymbol{e}_{\mathbf{d}}$ in (13) has a relative degree of 2

$$\ddot{\boldsymbol{e}}_{\mathbf{d}} = \dot{\mathbf{J}}_{\mathrm{d}}\boldsymbol{\alpha}_{\boldsymbol{q}_{\mathrm{d}}} + \mathbf{J}_{\mathrm{d}}\dot{\boldsymbol{\alpha}}_{\boldsymbol{q}_{\mathrm{d}}} - \ddot{\boldsymbol{s}}_{\mathrm{ref}}(t), \quad (16)$$

then, the input-output task dynamics is obtained such that

$$\dot{\boldsymbol{\eta}}_{\mathrm{d}} = \mathbf{A}_{\boldsymbol{\eta}_{\mathrm{d}}}\boldsymbol{\eta}_{\mathrm{d}} + \mathbf{B}_{\boldsymbol{\eta}_{\mathrm{d}}}\boldsymbol{\mu}, \quad (17)$$

$$\mathbf{A}_{\boldsymbol{\eta}_{\mathrm{d}}} = \begin{bmatrix}\mathbf{0} & \mathbf{I}_m \\ \mathbf{0} & \mathbf{0}\end{bmatrix}, \mathbf{B}_{\boldsymbol{\eta}_{\mathrm{d}}} = \begin{bmatrix}\mathbf{0} \\ \mathbf{I}_m\end{bmatrix}, \quad (18)$$

$$\boldsymbol{\mu} = \dot{\mathbf{J}}_{\mathrm{d}}\boldsymbol{\alpha}_{\boldsymbol{q}_{\mathrm{d}}} + \mathbf{J}_{\mathrm{d}}\dot{\boldsymbol{\alpha}}_{\boldsymbol{q}_{\mathrm{d}}} - \ddot{\boldsymbol{s}}_{\mathrm{ref}}(t). \quad (19)$$

$\boldsymbol{\mu} \in \mathbb{R}^m$ is the task-space control input affine in $\dot{\boldsymbol{\alpha}}_{\boldsymbol{q}_{\mathrm{d}}}$ (19). The control objective consists in formulating a task-space controller $\boldsymbol{\mu}$ that steers $\boldsymbol{\eta}$ to the origin.

C. Constraint Formulation with Barrier Functions

The general form of a constraint is expressed as

$$\mathrm{dist}(\boldsymbol{x}) \geq \mathrm{dist}_{\min}, \quad (20)$$

where $\mathrm{dist}(\boldsymbol{x}) \in \mathbb{R}$ is a distance obtained by forward kinematics and defined in the space of interest, see Fig. 1, and $\mathrm{dist}_{\min} \in \mathbb{R}$ is the threshold. Let us consider the set $\mathcal{C} = \{\boldsymbol{x} \in \mathbb{R}^{13+2n} : \ (20)\}$. The fulfillment of the constraint (20) forward in time can be checked by verifying the *forward invariance* of $\mathcal{C}$ [46] (see Appendix A). Barrier functions are a suitable tool for this purpose. In fact, considering the barrier function $h(\boldsymbol{x}) = \mathrm{dist}(\boldsymbol{x}) - \mathrm{dist}_{\min} \geq 0$, $\mathcal{C}$ is forward invariant if $h(\boldsymbol{x})$ satisfies Lyapunov-like conditions (see [3, Definition 3]) based on the system's dynamics. Rather than verifying the fulfillment of (20), one may be interested in finding the control input $\dot{\boldsymbol{\alpha}}_{\boldsymbol{q}_{\mathrm{d}}}$ that enforces (20) forward in time. Exponential Control Barrier Function (ECBF) allows to formulate a constraint on the control input that enforces the asymptotic stability of $\mathcal{C}$ and thereby its forward invariance. This constraint can be then accounted for in QP[6]For an extensive survey about barrier functions[7], see [48]. In Section IV-B,

[6]Conversely to $h(\boldsymbol{x}) \geq 0$ which does not depend on the decision variables.

[7]In the literature, there are reciprocal and zeroing barrier functions. They are equivalent to characterize forward invariance [3]. Albeit, zeroing barrier functions are convenient for robustness study [47].

we introduce the set robust stability, then we propose a robust formulation of ECBF that enforces this notion. First, we present in this section the basics of ECBF formulation to follow the same notations afterward.

1) Exponential Control Barrier Function: Let us define the sets $\mathcal{C}, \mathcal{C}_\mathrm{d} \subset \mathbb{R}^{13+2n}$ as

$$\mathcal{C} = \left\{ \boldsymbol{x} \in \mathbb{R}^{13+2n} : h(\boldsymbol{x}) \geq 0 \right\}, \tag{21}$$

$$\mathcal{C}_\mathrm{d} = \left\{ \boldsymbol{x}_\mathrm{d} \in \mathbb{R}^{13+2n} : h(\boldsymbol{x}_\mathrm{d}) \geq 0 \right\}. \tag{22}$$

Let us define the following states

$$\boldsymbol{\eta}^h_\mathrm{d}(\boldsymbol{x}_\mathrm{d}) = \begin{bmatrix} h_\mathrm{d} \\ \dot{h}_\mathrm{d} \end{bmatrix} = \begin{bmatrix} h_\mathrm{d} \\ \mathbf{J}^h_\mathrm{d} \boldsymbol{\alpha}_{\boldsymbol{q}_\mathrm{d}} \end{bmatrix} \in {}_\mathrm{b}H \subset \mathbb{R}^2, \tag{23}$$

$$\boldsymbol{\eta}^h(\boldsymbol{x}) = \begin{bmatrix} h \\ \dot{h} \end{bmatrix} = \begin{bmatrix} h \\ \mathbf{J}^h \boldsymbol{\alpha}_{\boldsymbol{q}} \end{bmatrix} \in {}_\mathrm{b}H \subset \mathbb{R}^2, \tag{24}$$

where $\mathbf{J}^h_\mathrm{d}, \mathbf{J}^h \in \mathbb{R}^{1\times(6+n)}$ are the barrier function Jacobians computed w.r.t $\boldsymbol{q}_\mathrm{d}$ and $\boldsymbol{q}$, respectively; $\boldsymbol{\eta}^h_\mathrm{d}(\boldsymbol{x}_\mathrm{d})$ and $\boldsymbol{\eta}^h(\boldsymbol{x})$ denote the desired and actual constraint dynamics states, respectively; ${}_\mathrm{b}H$ is the set of their admissible values.

As in (15), we have the following

$$\begin{aligned} &\boldsymbol{\eta}^h(\boldsymbol{x}) = \boldsymbol{\eta}^h_\mathrm{d}(\boldsymbol{x}_\mathrm{d}) + \boldsymbol{\eta}^h_{\boldsymbol{\phi}},\ \boldsymbol{\eta}^h_{\boldsymbol{\phi}} = \left.\tfrac{\partial \boldsymbol{\eta}^h(\boldsymbol{x})}{\partial \boldsymbol{x}}\right|_{\boldsymbol{x}=\check{\boldsymbol{x}}} \boldsymbol{\phi} \\ &\frac{\partial \boldsymbol{\eta}^h(\boldsymbol{x})}{\partial \boldsymbol{x}} = \begin{bmatrix} \mathbf{J}^h & \mathbf{0} \\ \frac{\partial (\mathbf{J}^h \boldsymbol{\alpha}_{\boldsymbol{q}})}{\boldsymbol{q}} & \mathbf{J}^h \end{bmatrix} \end{aligned}, \tag{25}$$

where $\boldsymbol{\eta}^h_{\boldsymbol{\phi}}$ is the mapping of $\boldsymbol{\phi}$ in the constraint-space. As in (15), Remark 2 is considered for $\left.\frac{\partial \boldsymbol{\eta}^h(\boldsymbol{x})}{\partial \boldsymbol{x}}\right|_{\boldsymbol{x}=\check{\boldsymbol{x}}} \boldsymbol{\phi}$ in (25).

Similarly to (16), h_d has a relative-degree of 2

$$\ddot{h}_\mathrm{d} = \dot{\mathbf{J}}^h_\mathrm{d} \boldsymbol{\alpha}_{\boldsymbol{q}_\mathrm{d}} + \mathbf{J}^h_\mathrm{d} \dot{\boldsymbol{\alpha}}_{\boldsymbol{q}_\mathrm{d}}. \tag{26}$$

Then as in (17), from (26) we get

$$\dot{\boldsymbol{\eta}}^{\boldsymbol{h}}_\mathbf{d} = \mathbf{A}_{\boldsymbol{\eta}^h_\mathrm{d}} \boldsymbol{\eta}^h_\mathrm{d} + \mathbf{B}_{\boldsymbol{\eta}^h_\mathrm{d}} \mu^h, \tag{27}$$

$$h_\mathrm{d} = \mathbf{C}_{\boldsymbol{\eta}^h_\mathrm{d}} \boldsymbol{\eta}^h_\mathrm{d}, \tag{28}$$

$$\mathbf{A}_{\boldsymbol{\eta}^h_\mathrm{d}} = \begin{bmatrix} 0 & 1 \\ 0 & 0 \end{bmatrix}, \mathbf{B}_{\boldsymbol{\eta}^h_\mathrm{d}} = \begin{bmatrix} 0 \\ 1 \end{bmatrix}, \mathbf{C}_{\boldsymbol{\eta}^h_\mathrm{d}} = \begin{bmatrix} 1 & 0 \end{bmatrix}, \tag{29}$$

$$\mu^h = \dot{\mathbf{J}}^h_\mathrm{d} \boldsymbol{\alpha}_{\boldsymbol{q}_\mathrm{d}} + \mathbf{J}^h_\mathrm{d} \dot{\boldsymbol{\alpha}}_{\boldsymbol{q}_\mathrm{d}}. \tag{30}$$

Let $\mu^h = -\mathbf{K}^h \boldsymbol{\eta}^h_\mathrm{d} \in \mathbb{R}$ with $\mathbf{K}^h = \begin{bmatrix} K^h_\mathrm{s} & K^h_\mathrm{d} \end{bmatrix} \in \mathbb{R}^{1\times 2}$. From (27) and (28), $h_\mathrm{d}(t) = \mathbf{C}_{\boldsymbol{\eta}^h_\mathrm{d}} \exp\left(\mathbf{F}_{\boldsymbol{\eta}^h_\mathrm{d}} t\right) \boldsymbol{\eta}^h_\mathrm{d}(t_0)$ with $\mathbf{F}_{\boldsymbol{\eta}^h_\mathrm{d}} = \mathbf{A}_{\boldsymbol{\eta}^h_\mathrm{d}} - \mathbf{B}_{\boldsymbol{\eta}^h_\mathrm{d}} \mathbf{K}^h$. Hence, if

$$\mu^h \geq -\mathbf{K}^h \boldsymbol{\eta}^h_\mathrm{d} \overset{(30)}{\iff} \dot{\mathbf{J}}^h_\mathrm{d} \boldsymbol{\alpha}_{\boldsymbol{q}_\mathrm{d}} + \mathbf{J}^h_\mathrm{d} \dot{\boldsymbol{\alpha}}_{\boldsymbol{q}_\mathrm{d}} \geq -\mathbf{K}^h \boldsymbol{\eta}^h_\mathrm{d}, \tag{31}$$

then following the Comparison Lemma [49, Lemma 3.4], $h_\mathrm{d}(t) \geq \mathbf{C}_{\boldsymbol{\eta}^h_\mathrm{d}} \exp\left(\mathbf{F}_{\boldsymbol{\eta}^h_\mathrm{d}} t\right) \boldsymbol{\eta}^h_\mathrm{d}(t_0)$. If there exists a gain matrix $\mathbf{K}^h$ such that $h_\mathrm{d}(t) \geq \mathbf{C}_{\boldsymbol{\eta}^h_\mathrm{d}} \exp\left(\mathbf{F}_{\boldsymbol{\eta}^h_\mathrm{d}} t\right) \boldsymbol{\eta}^h_\mathrm{d}(t_0) \geq 0$ whenever $h_\mathrm{d}(t_0) \geq 0$, then h_d is an ECBF, and $\mathcal{C}_\mathrm{d}$ is made forward invariant (also said 'safe') (see [48, Definition 7]). The gain matrix $\mathbf{K}^h$ needs to satisfy two specifications: (i) $\mathbf{F}_{\boldsymbol{\eta}^h_\mathrm{d}}$ eigenvalues must be real-negative, and (ii) $h_\mathrm{d}(t) \geq 0$, $\forall t \geq t_0$, $\forall \boldsymbol{x}_\mathrm{d}(t_0) \in \mathcal{C}_\mathrm{d}$ [5], [50]. Note that ECBF formulation (31) corresponds to the feedforward closed-loop QP control scheme in Fig. 4(b) where the non-modeled dynamics are not accounted for, and thereby (31) is called forward ECBF formulation.

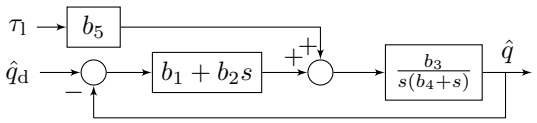

Fig. 6. 1-DoF joint-dynamics block scheme from which the system (35) is derived. It is DC motor servoed in position by a PD joint controller. The parameters $a_{i=1,\ldots,5}$ in Table I are as follows: $a_1 = -b_1 b_3$, $a_2 = -b_2 b_3 - b_4$, $a_3 = -a_1$, $a_4 = b_2 b_3$, $a_5 = b_3 b_5$. The latter show the coupling between the PD gains (b_1 and b_2) of the joint controller and the electro-mechanical constants (b_3, b_4 and b_5) of the DC motor. The systems 1 and 2 in Table I have the same electro-mechanical constants but different PD gains.

Unfortunately, it does not imply forward invariance of the set $\mathcal{C}_\mathrm{d}$ when the feedback closed-loop QP control scheme Fig. 4(a) is adopted as it will be shown in Section III-B. Hence, the goal is to formulate μ^h such that $\mathcal{C}_\mathrm{d}$ is made robustly stable.

D. Combining Tasks and Constraints via QP

Since (19) and (30) are affine in $\dot{\boldsymbol{\alpha}}_{\boldsymbol{q}_\mathrm{d}}$, the task and set $\mathcal{C}$ stabilization can be formulated and combined by the following weight-prioritized QP (highlighted terms are changed later)

$$\begin{aligned} \left[\dot{\boldsymbol{\alpha}}^*_{\boldsymbol{q}_\mathrm{d}}, \boldsymbol{f}^*\right] = \ & \arg\min \frac{w_0}{2} \left\| \mathbf{S} \dot{\boldsymbol{\alpha}}_{\boldsymbol{q}_\mathrm{d}} + \boldsymbol{\kappa}(\hat{\boldsymbol{x}}) \right\|^2 + \\ & \frac{w}{2} \left\| \mathbf{J}_\mathrm{d} \dot{\boldsymbol{\alpha}}_{\boldsymbol{q}_\mathrm{d}} + \dot{\mathbf{J}}_\mathrm{d} \boldsymbol{\alpha}_{\boldsymbol{q}_\mathrm{d}} - \ddot{\boldsymbol{s}}_\mathrm{ref}(t) \boldsymbol{-\mu} \right\|^2 \end{aligned} \tag{32a}$$

$$\text{s.t.} \quad (4), (5) \tag{32b}$$

$$-\mathbf{J}^h_\mathrm{d} \dot{\boldsymbol{\alpha}}_{\boldsymbol{q}_\mathrm{d}} \leq \dot{\mathbf{J}}^h_\mathrm{d} \boldsymbol{\alpha}_{\boldsymbol{q}_\mathrm{d}} \boldsymbol{-\mu^h} \tag{32c}$$

$$\mathbf{J}^\mathrm{c}_\mathrm{d} \dot{\boldsymbol{\alpha}}_{\boldsymbol{q}_\mathrm{d}} = -\dot{\mathbf{J}}^\mathrm{c}_\mathrm{d} \boldsymbol{\alpha}_{\boldsymbol{q}_\mathrm{d}} - k \mathbf{J}^\mathrm{c}_\mathrm{d} \boldsymbol{\alpha}_{\boldsymbol{q}_\mathrm{d}} \tag{32d}$$

where w and w_0 are positive weighting scalars such that $w \geq 0$ and $w_0 > 0$ [36, Lemma 2]. The first term in (32a) is a secondary task that solves the remaining redundancy where $\mathbf{S} = \begin{bmatrix} \mathbf{0}_{n\times 6} & \mathbf{I}_n \end{bmatrix}$[8] is a selection matrix and $\boldsymbol{\kappa}(\hat{\boldsymbol{x}})$ is a given joint-space feedback. Constraint (32d) stands for the no-slipping contacts (e.g., at the feet) to have, along with (5), feasible and dynamically-consistent floating-base solutions $\dot{\boldsymbol{\nu}}_\mathrm{d}$ where $\mathbf{J}^\mathrm{c}_\mathrm{d}$ is the contact Jacobian, and $k > 0$.

III. Instability of Feedback QP Control Scheme

Now, we show that formulating QP (32) according to the closed-loop control scheme in Fig. 4(a) may lead to instability.

A. Task Feedback Formulation

Let us formulate $\boldsymbol{\mu}$ as an output feedback control

$$\begin{aligned} &\boldsymbol{\mu} = -\mathbf{K}\boldsymbol{\eta},\ \mathbf{K} = \begin{bmatrix} \mathbf{K}_\mathrm{s} & \mathbf{K}_\mathrm{d} \end{bmatrix} \in \mathbb{R}^{m\times 2m}, \\ &(15) \Rightarrow \boldsymbol{\mu} = -\mathbf{K}\boldsymbol{\eta}_\mathrm{d} - \mathbf{K}\boldsymbol{\eta}_{\boldsymbol{\phi}}. \end{aligned} \tag{33}$$

By replacing (33) in (17), we get

$$\dot{\boldsymbol{\eta}}_\mathrm{d} = \mathbf{F}_{\boldsymbol{\eta}_\mathrm{d}} \boldsymbol{\eta}_\mathrm{d} - \mathbf{B}_{\boldsymbol{\eta}_\mathrm{d}} \mathbf{K} \boldsymbol{\eta}_{\boldsymbol{\phi}},\ \mathbf{F}_{\boldsymbol{\eta}_\mathrm{d}} = \mathbf{A}_{\boldsymbol{\eta}_\mathrm{d}} - \mathbf{B}_{\boldsymbol{\eta}_\mathrm{d}} \mathbf{K}, \tag{34}$$

where $\mathbf{K}$ is chosen such that $\mathbf{F}_{\boldsymbol{\eta}_\mathrm{d}}$ is Hurwitz, and $\mathbf{K}\boldsymbol{\eta}_{\boldsymbol{\phi}} \in \mathbb{R}^m$ is a perturbation term showing the coupling between the task gains and the effect of all the non-modeled dynamics $\boldsymbol{\eta}_{\boldsymbol{\phi}}$. By the virtue of Lyapunov's indirect method [49, Theorem 4.7],

[8]For a fixed-base robot, $\mathbf{S} = \mathbf{I}_n$.

TABLE I
PARAMETERS USED FOR SYSTEM (35) NUMERICAL SIMULATIONS.

	System 1	System 2	Units
a_1	-376.5977	-2380.6356	s^{-2}
a_2	-158.5073	-173.5712	s^{-1}
a_3	376.5977	2380.6356	s^{-2}
a_4	2.8245	17.8884	s^{-1}
a_5	4.7034	4.7034	rad / N.m.s^2

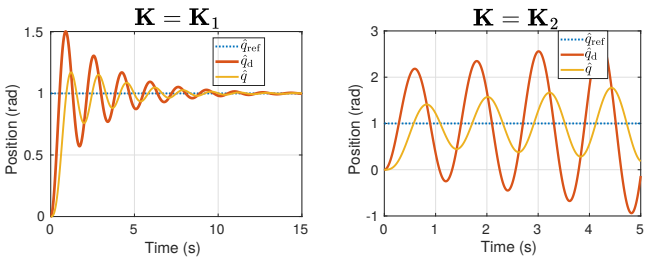

Fig. 7. Non-robustness of output feedback control (33) in system (35) with $\mathbf{K} = \mathbf{K}_1$ (left) and $\mathbf{K} = \mathbf{K}_2$ (right). Increasing the task gains with the same system parameters leads the closed-loop system to instability.

$\boldsymbol{\eta}_{\text{d}}$ is only locally stable for *sufficiently* bounded $\mathbf{K}\boldsymbol{\eta}_{\boldsymbol{\phi}}$. Otherwise, the closed-loop stability is not guaranteed.

To exemplify this claim, let us consider a 1-DoF system in Fig. 6 ($n = 1$, $\dot{\alpha}_{q_{\text{d}}} = \ddot{\hat{q}}_{\text{d}}$) governed by the following dynamics

$$\dot{\hat{\boldsymbol{x}}} = \begin{bmatrix} 0 & 1 \\ a_1 & a_2 \end{bmatrix} \hat{\boldsymbol{x}} + \begin{bmatrix} 0 & 0 \\ a_3 & a_4 \end{bmatrix} \hat{\boldsymbol{x}}_{\text{d}} + \begin{bmatrix} 0 \\ a_5 \end{bmatrix} \tau_{\text{l}}, \ \hat{\boldsymbol{x}} = \begin{bmatrix} \hat{q} \\ \dot{\hat{q}} \end{bmatrix} \in \mathbb{R}^2, \quad (35)$$

where $a_{i=\{1,\dots,5\}} \in \mathbb{R}$ denote the system parameters. The control objective is to drive the motor position $\hat{q}$ to reach a reference position $\hat{q}_{\text{ref}} = 1$ rad with no external disturbance ($\tau_{\text{l}} = 0$). Eqs. (13) and (14) become ($s(q) = \hat{q}$)

$$\boldsymbol{\eta}(\hat{\boldsymbol{x}}) = \begin{bmatrix} \hat{q} - \hat{q}_{\text{ref}} \\ \dot{\hat{q}} \end{bmatrix}, \ \boldsymbol{\eta}_{\text{d}}(\hat{\boldsymbol{x}}_{\text{d}}) = \begin{bmatrix} \hat{q}_{\text{d}} - \hat{q}_{\text{ref}} \\ \dot{\hat{q}}_{\text{d}} \end{bmatrix}, \ \mu = \ddot{\hat{q}}_{\text{d}} \in \mathbb{R}.$$

a_i are taken according to System 1 in Table I. Output feedback control (33) is performed (implemented on system (17)) with two sets of gains: $\mathbf{K}_1 = \begin{bmatrix} 10 & 2\sqrt{10} \end{bmatrix}$ and $\mathbf{K}_2 = \begin{bmatrix} 30 & 2\sqrt{30} \end{bmatrix}$. Figure 7 shows that simply increasing the task gains leads to instability of the closed-loop system. In Section IV-A, we propose a task feedback to ensure *global robust stability*.

B. Feedback ECBF Formulation

Let us consider the feedback QP control scheme in Fig. 4(a), ECBF constraint (31) becomes

$$\begin{aligned} \mu^h &\geq -\mathbf{K}^h \boldsymbol{\eta}^h, \\ \overset{(25)}{\iff} \mu^h &\geq -\mathbf{K}^h \boldsymbol{\eta}^h_{\text{d}} - \mathbf{K}^h \boldsymbol{\eta}^h_{\boldsymbol{\phi}}. \end{aligned} \quad (36)$$

As in Section III-A, feedback ECBF formulation (36) may not ensure the stability of sets $\mathcal{C}_{\text{d}}$ and $\mathcal{C}$ if the term $\mathbf{K}^h \boldsymbol{\eta}^h_{\boldsymbol{\phi}}$ is not sufficiently bounded; which shows the coupling between the ECBF gains and the disturbance $\boldsymbol{\eta}^h_{\boldsymbol{\phi}}$. In Fig. 8 we compare feedforward and feedback ECBF formulations where $h = 3 - \hat{q}$, $h_{\text{d}} = 3 - \hat{q}_{\text{d}}$ and a steady-state error $\hat{\phi} \neq 0$ is simulated by applying a constant disturbance $\tau_{\text{l}} = 5$ N.m. a_i parameters are taken according to System 2 in Table I and $\mathbf{K}^h$ is computed as in [5]. The task is formulated as in Section III-A except

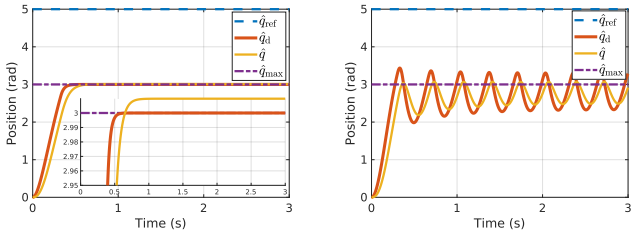

Fig. 8. ECBF formulation performed on system (35) in feedforward (31) (left) and feedback (36) (right) QP control schemes.

$\hat{q}_{\text{ref}} = 5$ rad. Feedforward ECBF (31) does not account for the disturbance which leads to a constraint violation. On the other hand, feedback ECBF (36) is not robust to non-modeled joint-dynamics resulting in sustained oscillations around the set boundary $\hat{q}_{\max} = 3$ rad. In Section IV-B, we propose a new formulation of μ^h to guarantee *robust stability* of $\mathcal{C}_{\text{d}}$.

IV. ROBUST FEEDBACK QP CONTROL FORMULATION

The proposed robust design of the QP controller consists of the following steps. The main result is given by Theorems 1 and 2 that show how $\boldsymbol{\mu}$ and μ^h are formulated including integral feedback terms to ensure $\boldsymbol{\eta}_{\text{d}}$ and $\boldsymbol{\eta}^h_{\text{d}}$ convergence to their respective residual sets, and thereby their boundedness. Then, Proposition 1 makes the bridge between the desired task-space state $\boldsymbol{\eta}_{\text{d}}$ and the corresponding desired robot state $\boldsymbol{x}_{\text{d}}$ by showing that if the former is bounded so is the latter. Finally, based on Assumption 1 and Proposition 1, Proposition 2 establishes the boundedness relationship between $\boldsymbol{\eta}_{\text{d}}$ and $\boldsymbol{\eta}$.

Proposition 1. *If $\boldsymbol{\eta}_{\text{d}}$ (resp. $\boldsymbol{\eta}^h_{\text{d}}$) is bounded, so is $\boldsymbol{x}_{\text{d}}$.*

Proof. See Appendix B. □

Proposition 2. *If $\boldsymbol{\eta}_{\text{d}}$ (resp. $\boldsymbol{\eta}^h_{\text{d}}$) is (uniformly) ultimately bounded then $\boldsymbol{\eta}$ (resp. $\boldsymbol{\eta}^h$) is (uniformly) ultimately bounded.*

Proof. See Appendix C. □

Let us introduce the following states

$$\begin{aligned} \boldsymbol{\psi} &= \begin{bmatrix} \boldsymbol{e}^\intercal & \dot{\boldsymbol{e}}^\intercal & \dot{\boldsymbol{e}}^\intercal_{\mathbf{d}} \end{bmatrix}^\intercal, \ \boldsymbol{\psi} \in \Psi \subset \mathbb{R}^{3m}, \\ \boldsymbol{\psi}^h &= \begin{bmatrix} h^\intercal & \dot{h}^\intercal & \dot{h}^\intercal_{\text{d}} \end{bmatrix}^\intercal, \ \boldsymbol{\psi}^h \in \Psi^h \subset \mathbb{R}^3, \end{aligned}$$

where Ψ and Ψ^h are the admissible values of $\boldsymbol{\psi}$ and $\boldsymbol{\psi}^h$, respectively; they are used for $\boldsymbol{\mu}$ and μ^h formulations, resp.

A. Global Robust Stable Task Formulation

When the solutions of (17) converge to a residual set $\Omega \subset H$ with $0 \in \Omega$ for all initial conditions and admissible perturbations, $\boldsymbol{\eta}_{\text{d}}$ is said to be Robustly Globally Uniformly Asymptotically Stable w.r.t Ω (RGUAS-Ω). The robust stabilization problem consists in finding $\boldsymbol{\mu}$ such that $\boldsymbol{\eta}_{\text{d}}$ is RGUAS-Ω. If Ω can be made arbitrarily small (but still not equal to the origin), $\boldsymbol{\eta}_{\text{d}}$ is said to be robustly *practically* stable (see Definition in Appendix A). An illustrative scheme of RGUA-Stability is shown in Fig. 9. In the following, we state the main result of this subsection.

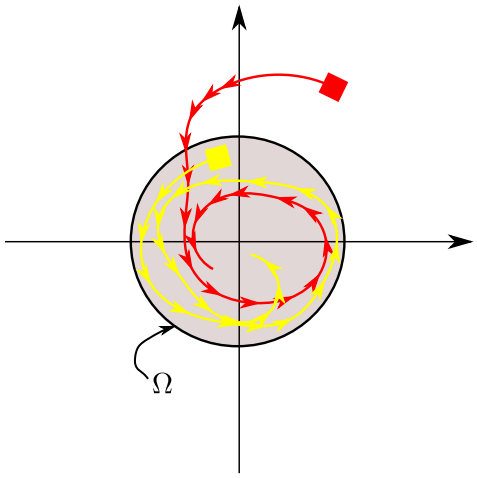

Fig. 9. RGUAS-Ω illustrative scheme. Two state trajectories are shown: the red one starts (squares) outside the residual set Ω then it converges to Ω over time, whereas the yellow one starts inside Ω and remains within it.

Theorem 1. *Let us assume that $\boldsymbol{\eta}_{\boldsymbol{\phi}}$ is bounded. If*

$$\boldsymbol{\mu} = -\mathbf{L}\boldsymbol{\psi},\ \mathbf{L} = \begin{bmatrix}\mathbf{K}_\mathrm{s} & \mathbf{K}_\mathrm{d} & \mathbf{K}_\mathrm{i}\end{bmatrix} \in \mathbb{R}^{m\times 3m}, \tag{37}$$

where $\mathbf{K}_\mathrm{s}, \mathbf{K}_\mathrm{i} \in \mathbb{R}^{m\times m}$ are diagonal positive-definite matrices, and $\mathbf{K}_\mathrm{d}$ chosen such that $\check{\mathbf{F}}_{\boldsymbol{\eta}_\mathrm{d}} = \mathbf{A}_{\boldsymbol{\eta}_\mathrm{d}} - \mathbf{B}_{\boldsymbol{\eta}_\mathrm{d}}\check{\mathbf{K}}$ is Hurwitz, with $\check{\mathbf{K}} = [\mathbf{K}_\mathrm{s} \quad \mathbf{K}_\mathrm{d} + \mathbf{K}_\mathrm{i}]$, then there exists $\mathbf{K}_\mathrm{i}$ such that $\boldsymbol{\eta}_\mathrm{d}$ is robustly practically stable.

Proof. See Appendix D. □

From Proposition 2 and Theorem 1, $\boldsymbol{\eta}$ is uniformly ultimately bounded with ultimate bound $\tilde{\varrho}$. Comparatively to (33), (37) penalizes the integral term $\dot{\boldsymbol{e}}_\mathbf{d}(t) = \int_0^t \boldsymbol{\mu}(s)ds$ growth ensuring the desired task state $\boldsymbol{\eta}_\mathrm{d}$ is bounded despite the presence of disturbances and non-modeled dynamics $\boldsymbol{\eta}_{\boldsymbol{\phi}}$. This is the key feature for robust stability. The '*global*' property comes from the fact that stability is ensured for every bounded $\mathbf{K}\boldsymbol{\eta}_{\boldsymbol{\phi}}$ whereas in (34) it is required to be '*sufficiently*' bounded. Also, the '*practical*' aspect denotes the ability of the integral gain (that can be tuned independently from the stiffness and damping) to reduce the effect of the perturbation as shown in (67) making the residual set $\Omega_{\boldsymbol{\eta}_\mathrm{d}}$ arbitrarily small. Nevertheless, (67) does only prove the existence of a set of integral gains $\mathbf{K}_\mathrm{i}$ enforcing robust stability without providing a constructive method to compute them. In practice, we do not know the task stiffness that will turn the closed-loop system instable as it depends on the executed task and the robot non-modeled joint-dynamics. Hence, the necessary amount of integral gain for robust stability is not known *a priori*.

To show the effect of the integral gains on the closed-loop system dynamics, let us take the system in Section III-A with the instable configuration (see Fig. 7) and add the integral feedback term. Figure 10(a) shows that low integral gain values do not achieve robust stability since the condition (67) is not satisfied. If the integral gain is increased, robust stability is recovered, as shown in Fig. 10(b), but oscillations still exist at the reference target $\hat{q}_\mathrm{ref}$. These oscillations can be damped by increasing the integral gain to smoothly reach $\hat{q}_\mathrm{ref}$ while counterbalancing the external perturbation (Fig. 10(c)). Figure 10(d) shows that further increasing the integral gain overdamps the system response. The convergence smoothness is preserved at the expense of a higher settling time.

Another interesting aspect is that $\check{\mathbf{F}}_{\boldsymbol{\eta}_\mathrm{d}}$ being Hurwitz implies that $\mathbf{K}_\mathrm{d}$ can be chosen negative-definite as long as $\mathbf{K}_\mathrm{d} + \mathbf{K}_\mathrm{i}$ is positive-definite. Indeed, let us assume $\mathbf{K}_\mathrm{d} < 0$ and $\mathbf{K}_\mathrm{i} = \varepsilon|\mathbf{K}_\mathrm{d}|$ (element-wise) with $\varepsilon = 1+\varepsilon_0, \varepsilon_0 > 0$ yielding to

$$\begin{aligned}\boldsymbol{\mu} &= -\mathbf{K}_\mathrm{s}\boldsymbol{e} - \mathbf{K}_\mathrm{d}\dot{\boldsymbol{e}} - \mathbf{K}_\mathrm{i}\dot{\boldsymbol{e}}_\mathbf{d},\\ &= -\mathbf{K}_\mathrm{s}\boldsymbol{e} - \varepsilon_0|\mathbf{K}_\mathrm{d}|\dot{\boldsymbol{e}}_\mathbf{d} - |\mathbf{K}_\mathrm{d}|(\dot{\boldsymbol{e}}_\mathbf{d} - \dot{\boldsymbol{e}}),\end{aligned} \tag{38}$$

ε_0 is tuned to meet robustness condition (67). Eq. (38) shows that $\dot{\boldsymbol{e}}_\mathbf{d}$ is enforced to converge to zero while drifting toward $\dot{\boldsymbol{e}}$ due to $(\dot{\boldsymbol{e}}_\mathbf{d} - \dot{\boldsymbol{e}})$ feedback term. This is similar to the leaky-integrator proposed in [20] when (38) is performed in joint-space (i.e., posture task). Our claim is that performing a *task-space* integral feedback is more intuitive and enables a better understanding of the underlying conditions on task gains tuning while not affecting the QP solution optimality[9]. It also enables robust stability of each task in multi-objective control case, see Section IV-C (Proposition 3).

The term $(\dot{\boldsymbol{e}}_\mathbf{d} - \dot{\boldsymbol{e}})$ in (38) induces compliance w.r.t robot response in terms of velocity. Figure 11 shows this behavior. When the external disturbance is applied, the desired task velocity $\dot{\hat{q}}_\mathrm{d}$ immediately converges to zero in Fig. 11(a). Conversely, $\dot{\hat{q}}_\mathrm{d}$ drifts first toward $\dot{\hat{q}}$ (since the amplitude of $(\dot{\hat{q}}_\mathrm{d} - \dot{\hat{q}})$ is predominant) then converges back to zero in Fig. 11(b). In terms of position, the desired task position $\hat{q}_\mathrm{d}$ slightly drifts toward $\hat{q}$ then counterbalances the external disturbance. This feature is exploited in Section V-B.

Note that by setting $\mathbf{K}_\mathrm{i} = \mathbf{0}$, the output feedback (33) is recovered. Namely, the proposed approach does not constitute a substantial modification of the QP controller.

In the next subsection, we take inspiration from (37) to formulate Robust ECBF (RECBF) to enforce set robust stability.

B. Set Robust Stability Formulation

Let us define the sets $\mathcal{C}_\sigma, \mathcal{C}_{\mathrm{d}\sigma} \subset \mathbb{R}^{13+2n}$ with $\sigma \geq 0$

$$\mathcal{C}_\sigma = \left\{\boldsymbol{x} \in \mathbb{R}^{13+2n} : h + \sigma \geq 0\right\}, \tag{39}$$

$$\mathcal{C}_{\mathrm{d}\sigma} = \left\{\boldsymbol{x}_\mathrm{d} \in \mathbb{R}^{13+2n} : h_\mathrm{d} + \sigma \geq 0\right\}. \tag{40}$$

Before introducing the main result of this subsection, we define set robust stability and RECBF. The former is illustrated in Fig. 12.

Definition 1. *A closed set $\mathcal{S} \subset \mathbb{R}^{13+2n}$ is said to be* robustly stable *for a forward complete system* (7) *if $\exists\ \sigma \geq 0$, a closed and forward invariant set $\mathcal{S}_\sigma \subset \mathbb{R}^{13+2n}$, and an open $\mathcal{R} \subseteq \mathbb{R}^{13+2n}$ with $\mathcal{S} \subseteq \mathcal{S}_\sigma \subset \mathcal{R}$ such that $\mathcal{S}_\sigma$ is asymptotically stable.*

Let us now define RECBF to enforce set robust stability.

Definition 2. *Given a set $\mathcal{C}_\mathrm{d} \subset \mathbb{R}^{13+2n}$ defined as the superlevel set of a 2-times continuously differentiable function*

[9]In [20], feedback term related to $(\dot{\boldsymbol{e}}_\mathbf{d} - \dot{\boldsymbol{e}})$ is added to $\dot{\boldsymbol{\alpha}}_{\boldsymbol{q}_\mathrm{d}}$ post QP computation, and thereby it may not be feasible. Moreover, only experimental observations have been reported about the effect of the joint-space leaky integrator gain without any explicit condition on its values.

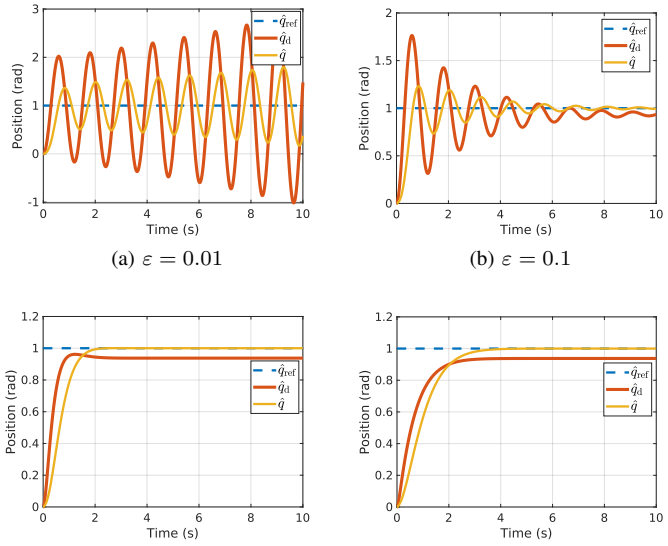

(a) $\varepsilon = 0.01$ (b) $\varepsilon = 0.1$

(c) $\varepsilon = 1$ (d) $\varepsilon = 2$

Fig. 10. System (35) response, with a_i of System 1 in Table I and $\tau_{\rm l} = 5$ N.m, under heterogeneous feedback (37). The integral gain $K_{\rm i} = \varepsilon K_{\rm d}$. This choice follows the fact that both $K_{\rm i}$ and $K_{\rm d}$ act on velocity terms.

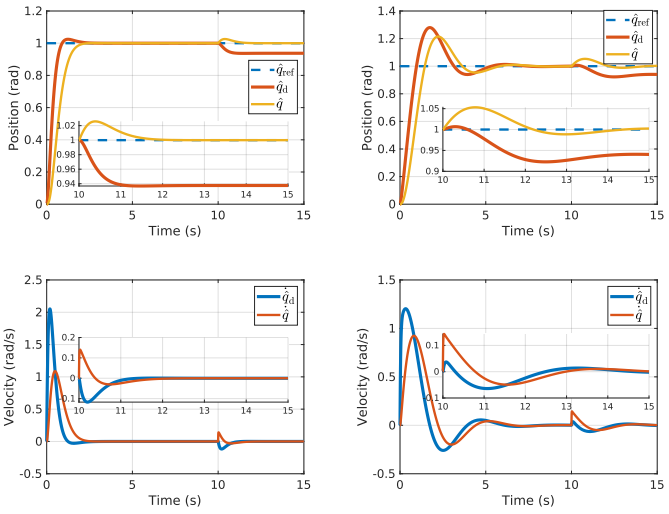

(a) (b)

Fig. 11. System (35) response, with a_i of System 1 in Table I, $\tau_{\rm l} = 5$ N.m is applied at $t = 10$ s, under heterogeneous feedback (37). (a) $\mu = \ddot{\hat{q}}_{\rm d} = -K_{\rm s}\hat{q} - K_{\rm d}\dot{\hat{q}} - K_{\rm i}\dot{\hat{q}}_{\rm d}$, $K_{\rm s} = 30$, $K_{\rm d} = 2\sqrt{K_{\rm s}}$, $K_{\rm i} = K_{\rm d}$. (b) $\mu = \ddot{\hat{q}}_{\rm d} = -K_{\rm s}\hat{q} - K_{\rm i}\dot{\hat{q}}_{\rm d} - |K_{\rm d}|\left(\dot{\hat{q}}_{\rm d} - \dot{\hat{q}}\right)$, $K_{\rm s} = 30$, $K_{\rm d} = -1.8\sqrt{K_{\rm s}}$, $K_{\rm i} = 3.2\sqrt{K_{\rm s}}$.

$h_{\rm d} : \mathbb{R}^{13+2n} \to \mathbb{R}$, then $h_{\rm d}$ is a RECBF if there exists $\mu^h \in \mathbb{R}$ such that for (7),

$$\sup_{\dot{\boldsymbol{\alpha}}_{\boldsymbol{q}_{\rm d}} \in \mathcal{U}} \left[\dot{\mathbf{J}}^h_{\rm d} \boldsymbol{\alpha}_{\boldsymbol{q}_{\rm d}} + \mathbf{J}^h_{\rm d} \dot{\boldsymbol{\alpha}}_{\boldsymbol{q}_{\rm d}} + \mu^h \right] \geq 0, \tag{41}$$

results in $\mathcal{C}_{\rm d}$ is robustly stable.

Inspiring from Theorem 1, Theorem 2 proposes a formulation for μ^h that guarantees the robust stability of $\mathcal{C}_{\rm d}$.

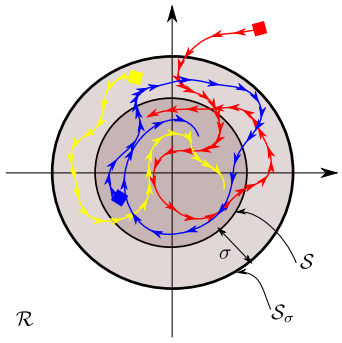

Fig. 12. The sets $\mathcal{S}$, $\mathcal{S}_\sigma$ and $\mathcal{R}$. $\mathcal{R}$ is open, $\mathcal{S}_\sigma$ is asymptotically stable and forward invariant, and $\mathcal{S}$ is robustly stable. If $\sigma = 0$, $\mathcal{S}$ and $\mathcal{S}_\sigma$ coincide. The colored trajectories denote three possible cases depending on the initial condition: in $\mathcal{R}$ (red), in $\mathcal{S}_\sigma$ (yellow), and in $\mathcal{S}$ (blue): the red one converges to $\mathcal{S}_\sigma$ and remains inside because of the set asymptotic stability; the yellow one cannot go out of $\mathcal{S}_\sigma$ because it is forward invariant; finally the blue one can slightly go out of $\mathcal{S}$ but remains inside $\mathcal{S}_\sigma$ (robust stability).

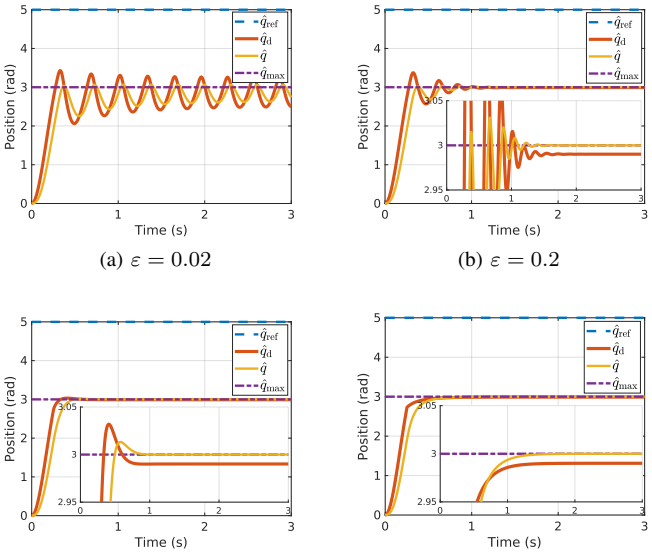

(a) $\varepsilon = 0.02$ (b) $\varepsilon = 0.2$

(c) $\varepsilon = 2$ (d) $\varepsilon = 5$

Fig. 13. System (35) response with a_i parameters of System 2 in Table I with $\tau_{\rm l} = 5$ N.m, under RECBF (42) with $K^h_{\rm i} = \varepsilon K^h_{\rm d}$.

Theorem 2. *Let us assume $\boldsymbol{\eta}^h_{\boldsymbol{\phi}}$ bounded. If*

$$\mu^h \geq -\mathbf{L}^h \boldsymbol{\psi}^h, \ \mathbf{L}^h = \begin{bmatrix} K^h_{\rm s} & K^h_{\rm d} & K^h_{\rm i} \end{bmatrix}, \tag{42}$$

where $K^h_{\rm i} > 0$ and $\check{\mathbf{K}}^h = \begin{bmatrix} K^h_{\rm s} & K^h_{\rm d} + K^h_{\rm i} \end{bmatrix} \in \mathbb{R}^{1\times 2}$ is chosen according to ECBF definition in Section II-C1, then there exists $K^h_{\rm i}$ such that $h_{\rm d}$ in (28) *is a RECBF, and the set $\mathcal{C}_{\rm d}$ is robustly stable.*

Proof. See Appendix E. □

By virtue of Proposition 2 and following from Theorem 2, $\boldsymbol{\eta}^h$ is uniformly ultimately bounded with ultimate bound $\tilde{\sigma}$ and thereby it converges to asymptotically stable set $\mathcal{C}_\sigma$ defined as (39). Hence, the set $\mathcal{C}$ is rendered robustly stable as well.

Remark 3. *Conceptually, Theorem 2 proposes the same solution as Theorem 1 and that is why the robustness conditions* (67) *and* (76) *are similar. This is because Theorem 2 does*

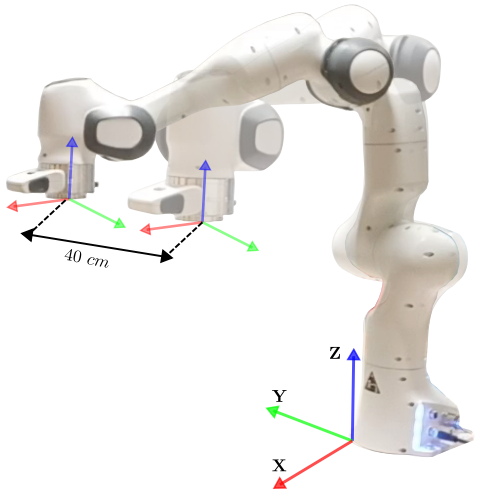

Fig. 14. Two superposed snapshots showing Panda end-effector converging to the two defined set-point pose targets.

only perceive the 'origin' slightly different from Theorem 1: the former considers it as a 'set' whereas the latter perceives it as a 'point'. This fact can also be seen from Figs. 9 and 12: shrinking the set $\mathcal{S}$ to the origin in the latter directly brings us to the former. Hence, the task gains properties discussed for (37) *apply as well to the RECBF constraint gains in* (42).

As in Fig. 10, Fig. 13 shows the conservativeness of tuning the RECBF integral gain K_{i}^h, where the same scenario in Section III-B is performed. Low K_{i}^h values do not ensure robust stability. Increasing K_{i}^h leads to meet the robustness condition (76), and thereby damp the oscillations at the set boundary. Further increasing K_{i}^h helps to remove the oscillations but at the expense of slower convergence to the boundary. The latter requires high deceleration amount especially that RECBF constraint (42) is only inserted in QP at the neighborhood of $\mathcal{C}$ boundary[10].

C. Weight-Prioritized Multi-Objective Robust QP Formulation

By replacing (37) and (42) in (32a) and (32c), respectively, the weight-prioritized multi-objective robust QP writes as

$$\left[\dot{\boldsymbol{\alpha}}_{\boldsymbol{q}_{\mathrm{d}}}^{*}, \boldsymbol{f}^{*}\right] = \arg\min \frac{w_0}{2}\left\|\mathbf{S}\dot{\boldsymbol{\alpha}}_{\boldsymbol{q}_{\mathrm{d}}} + \boldsymbol{\kappa}(\hat{\boldsymbol{x}})\right\|^2 + \frac{1}{2}\sum_{j=1} w_j \left\|\mathbf{J}_{\mathrm{d}}^j\dot{\boldsymbol{\alpha}}_{\boldsymbol{q}_{\mathrm{d}}} + \dot{\mathbf{J}}_{\mathrm{d}}^j\boldsymbol{\alpha}_{\boldsymbol{q}_{\mathrm{d}}} - \ddot{\boldsymbol{s}}_{\mathrm{ref}}^j(t) + \mathbf{L}^j\boldsymbol{\psi}^j\right\|^2 \tag{43a}$$

$$\text{s.t.} \quad (4), (5) \tag{43b}$$

$$-\mathbf{J}_{\mathrm{d}}^h\dot{\boldsymbol{\alpha}}_{\boldsymbol{q}_{\mathrm{d}}} \leq \dot{\mathbf{J}}_{\mathrm{d}}^h\boldsymbol{\alpha}_{\boldsymbol{q}_{\mathrm{d}}} + \mathbf{L}^h\boldsymbol{\psi}^h \tag{43c}$$

$$\mathbf{J}_{\mathrm{d}}^{\mathrm{c}}\dot{\boldsymbol{\alpha}}_{\boldsymbol{q}_{\mathrm{d}}} = -\dot{\mathbf{J}}_{\mathrm{d}}^{\mathrm{c}}\boldsymbol{\alpha}_{\boldsymbol{q}_{\mathrm{d}}} - k\mathbf{J}_{\mathrm{d}}^{\mathrm{c}}\boldsymbol{\alpha}_{\boldsymbol{q}_{\mathrm{d}}} \tag{43d}$$

with j indexing the task $\boldsymbol{s}^j$. From the structural standpoint, the proposed robust QP (43) is similar to the classical weighted-prioritized templated QP (32). Our contribution is in modifying the task and constraint formulations based on the sum of stiffness and damping terms (computed based on the robot measurements) to include feedback integral terms (computed based on the desired robot state). Our robust formulation does not call for a substantial modification in the QP formulation as in [15], nor for much additional computation as the integral terms are obtained by forward velocity, see Fig. 5.

Relatively to (32a), (43a) shows that the robust task formulation (37) is straightforwardly extended to the multi-task case where the integral term corresponding to each task $\boldsymbol{s}^j$ is added. Due to the subsequent conflicts that may arise between the different tasks, $\boldsymbol{s}^j$ is likely to be achieved partially according to its associated weight $w_j \geq 0$ and the potential active constraints[11] in QP (43). This implicit relaxation writes

$$\boldsymbol{\mu}^j = -\mathbf{L}^j\boldsymbol{\psi}^j + \boldsymbol{\delta}^j(t), \tag{44}$$

with $\boldsymbol{\delta}^j(t) \in \mathbb{R}^m$ assumed bounded $\left\|\boldsymbol{\delta}^j(t)\right\| \leq \delta_{\max}^j, \ \forall t \geq 0$. Proposition 3 generalizes Theorem 1 to the multi-task case.

Proposition 3. *Consider* (44) *such that Theorem 1 conditions hold. Then, there exists $\mathbf{K}_{\mathrm{i}}^j \in \mathbb{R}^{m\times m}$ positive-definite such that $\boldsymbol{\eta}_{\mathrm{d}}^j$ is practically robustly stable.*

Proof. See Appendix F. □

Note that thanks to Propositions 1 and 3 and Theorem 2, $\boldsymbol{x}_{\mathrm{d}}$ is bounded after double integration of $\dot{\boldsymbol{\alpha}}_{\boldsymbol{q}_{\mathrm{d}}}$ solution of (43).

Remark 4. *In* (43)*, only one RECBF constraint is considered. In the more general case, the QP constraints set encompasses: (i) several RECBFs (joint constraints, collision avoidance, CoM equilibrium region, etc.), and (ii) explicit bounds on $\ddot{\boldsymbol{q}}_{\mathrm{d}}$. Therefore, we highlight two important aspects: First, Theorem 2 assumes that $\mathcal{U} = \mathbb{R}^{6+n}$ which may not hold. Second, since all the constraints have the same level of priority, the QP will be infeasible if these constraints are in conflict (incompatible, i.e., empty feasibility domain) [51]–[53].*

V. Experimental Results and Discussion

To assess our robust QP controller and demonstrate its applicability to different use-cases, experiments are conducted with two different robots: a fixed-base 7-DoF robotic arm Panda from Franka Emika, and a (floating-base) 34-DoF humanoid robot HRP-4 from Kawada Robotics. The latter is controlled in position at a frequency of 200 Hz, whereas the former can be controlled either in position or in velocity modes at a control frequency of 1 kHz.

Both robots are controlled using the open source code implementation of the QP controller `mc_rtc`[12] with LSSOL solver. It includes a user task specification interface, debugging, data recording... for simulation as well as for real-time control. Based on the embedded sensors data (encoders, IMU, Force/Torque (F/T) sensors...), `mc_rtc` builds at each control-cycle the QP problem, based on user-defined tasks and constraints, and solves it. The QP decision variables are $\dot{\boldsymbol{\alpha}}_{\boldsymbol{q}_{\mathrm{d}}}$ and the contact forces $\boldsymbol{f}$.

[10]The number of rows of the constraint matrix is increased in consequence. This is very usual/common in our controller which is based on a Finite State Machine (FSM) which role is to elect the tasks and constraints depending on the current goals.

[11]An inequality constraint is active if it is enforced as equality.

[12]https://jrl-umi3218.github.io/mc_rtc/index.html

As it is shown in (7) and Fig. 5, $\dot{\boldsymbol{\alpha}}_{\boldsymbol{q}_\mathrm{d}}$ is integrated twice to obtain $\boldsymbol{x}_\mathrm{d}$, then the joint commands $\hat{\boldsymbol{x}}_\mathrm{d}$ are sent to the actuated joint controllers. $\dot{\hat{\boldsymbol{q}}}$ is estimated using numerical derivation for HRP-4, whereas it is readily available in the Franka Control Interface (FCI) for Panda[13]. The floating-base state $\boldsymbol{x}^\mathrm{FB}$ of HRP-4 is estimated by a built-in kinematic-inertial observer based on an extended filter. The control is performed using a laptop Dell Precision 5540 with Intel Xeon(R) E-2276M processor (CPU 12×2.80 GHz) and 32 GB of RAM running under Linux Ubuntu 18.04.5 LTS.

A. Task Robust Stability

Tasks gains correlate to accuracy (performing motions with high precision) and execution speed (controlling the overall task time). Consequently, performing fast and precise motion requires increasing the task gains which leads to instability. In this context, the Panda end-effector is controlled to perform a pick-and-place-like motion. Two set-point targets (position and orientation) are defined (to which the end-effector converges back and forth); $\dot{\hat{\boldsymbol{q}}}_\mathrm{d}$ is the input command for the joint controllers. To have simple plots, only the target coordinate along the Y-axis varies with an amplitude of ± 20 cm (Fig. 14).

QP (43) is formulated (the notations in Remark 1 are followed). such that the constraint set contains the kinematic constraints (joint-position and velocity constraints [5]); whereas, for comparison purpose, the task is formulated using: (i) output feedback (33), (ii) heterogeneous feedback (37). The task gains are set as $\mathbf{K}_\mathrm{d} = 2\sqrt{\mathbf{K}_\mathrm{s}}$ and $\mathbf{K}_\mathrm{i} = \varepsilon \mathbf{K}_\mathrm{d}$ with $\varepsilon = 0$ for (33) and $\varepsilon = 1$ for (37). Since we do not know *a priori* the task stiffness that will turn the closed-loop system instable, $\mathbf{K}_\mathrm{s}$ is initially set to $400\mathbf{I}$, then it is increased over time by increments of $50\mathbf{I}$ ($\mathbf{K}_\mathrm{d}$ and $\mathbf{K}_\mathrm{i}$ are updated accordingly).

Figure 15 shows the experiment results. For $\mathbf{K}_\mathrm{s} \leq 450\mathbf{I}$, both feedback controls (33) and (37) lead to stable convergence to the targets. However, for $\mathbf{K}_\mathrm{s} = 500\mathbf{I}$, the closed-loop system with output feedback (33) becomes instable (Fig. 15(a)) where strong oscillations and jerky motion appear at the end-effector mostly visible along the Z-axis (Fig. 17). This chattering can be very dangerous for the robot (accelerating drastically the wear of actuators and robot's structure) and the surrounding people or objects in the robot's neighborhood. Conversely, heterogeneous feedback (37) allows reaching robustly the targets while $\mathbf{K}_\mathrm{s}$ keeps increasing up to $850\mathbf{I}$ (Fig. 15(b)).

Increasing the task gains results in high values of desired joint acceleration $\ddot{\hat{\boldsymbol{q}}}_\mathrm{d}$ (Fig. 15(c)–(d)) which generates desired joint commands $\dot{\hat{\boldsymbol{q}}}_\mathrm{d}$ with fast variations that can not be well tracked by the joint controllers (Fig. 16(a)–(b)) due to the different rate limitations (acceleration, jerk) and the limited bandwidth. This leads to increase the joint tracking error $\boldsymbol{\phi}$ in (8), and correspondingly its task-space mapping $\boldsymbol{\eta}_{\boldsymbol{\phi}}$ in (15). Consequently, if the perturbation term $\mathbf{K}\boldsymbol{\eta}_{\boldsymbol{\phi}}$ is not sufficiently bounded, the closed-loop system under output feedback (19) is instable. In particular, adding the task-space integral term in (37) allows to withstand the perturbation by the gain $\mathbf{K}_\mathrm{i}$ as shown in (67) enforcing $\boldsymbol{\eta}_\mathrm{d}$ to remain bounded which leads to the boundedness of $\hat{\boldsymbol{x}}_\mathrm{d}$ (by virtue of Proposition 1).

[13]The FCI joint-velocity estimation is a low-pass filtered finite-difference.

In Fig. 15(b)–(d), we decided to stop at stiffness $\mathbf{K}_\mathrm{s} = 850\mathbf{I}$ as, due to hardware limits, further increasing the task gains has no effect on the convergence performance (Fig. 16(b)). Although the joint controllers reached their maximum tracking performances, our approach enables a stable motion even though the task gains keep increasing and imposing desired dynamics that cannot be performed by the robot. Hence, the closed-loop stability has to be ensured whatever the task gains and the joint-dynamics. Yet, ensuring the stability goes at the expanse of $\mathbf{K}_\mathrm{i}$ conservative tuning.

B. Set Robust Stability

Among usual safety constraints common to all robots such as joint limits and self-collisions avoidance that are implemented here as extension of [5], a critical safety feature in humanoids is enforcing balance, which is given a higher priority over manipulation tasks. When there are no contact transitions, constraining the CoM position from acceleration bounds enforces robust balance [54]. For co-planar feet contact, it is enough to confine the CoM of the HRP-4 humanoid robot to remain inside a conservative polygon (Fig. 18) such that its boundaries are reached with zero CoM velocity and acceleration. It is a conservative balance region because it is a subset of 3D balance set (polyhedron in multi-contact or prism in co-planar) that we use mainly for validation purpose. The robot CoM is pushed to the polygon boundaries by defining a sequence of Cartesian targets for the right hand to be reached. Rubber bushes and dampers are present under the robot ankles to absorb impacts at the feet while walking (Fig. 19). This shock-absorbing mechanism creates non-modeled underdamped flexibilities between the ankles and the feet. The latter are often observed in the form of small passive oscillations at the ankles which amplify through the whole structure. Their effect is not observed at the joints' encoders, but at the floating base state estimation (based on IMU measurements). Nevertheless, the joint feedback is used (along with the floating base state) to compute CoM Cartesian position and linear velocity. Moreover, the floating-base IMU noise affects the CoM estimation (denoted $\mathbf{CoM}(\boldsymbol{x}) \in \mathbb{R}^3$).

The robot CoM is constrained to be within the balance polygon by defining inequality constraints on the distance between the CoM and the polygon features. The 3D case would simply result in more inequalities constraining the CoM within a precomputed polyhedron [54]. The barrier functions h^i and h^i_d corresponding to each balance polygon feature i are

$$h^i = {\boldsymbol{n}^i}^\mathsf{T} \mathbf{CoM}(\boldsymbol{x}) + \Delta^i, \tag{45}$$

$$h^i_\mathrm{d} = {\boldsymbol{n}^i}^\mathsf{T} \mathbf{CoM}(\boldsymbol{x}_\mathrm{d}) + \Delta^i, \tag{46}$$

where $\boldsymbol{n}^i \in \mathbb{R}^3$ is the i^th feature's normal vector and $\Delta^i \in \mathbb{R}$ is the distance at which the feature is placed w.r.t the origin along $\boldsymbol{n}^i$. From (45)–(46), the sets $\mathcal{C}^i$ and $\mathcal{C}^i_\mathrm{d}$ are defined as in (21) and (22), respectively. QP (43) is formulated to steer the right hand to its targets while the constraints set contains the contact forces constraint (5) and non-slipping contacts (43d).

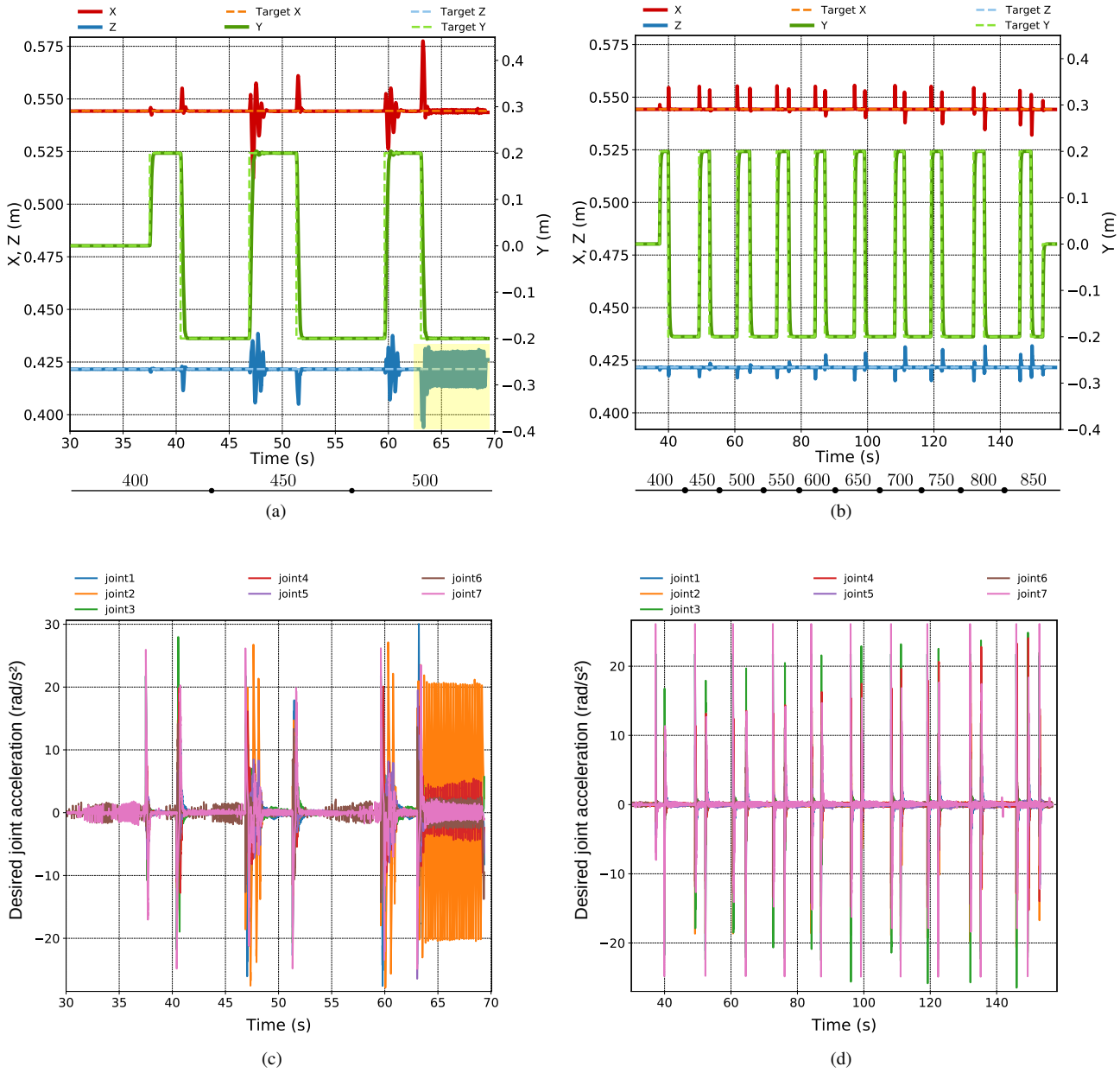

Fig. 15. Panda response for the 'pick-and-place' task under different feedback controls. End-effector Cartesian coordinates and $\ddot{\boldsymbol{q}}_{\mathrm{d}}$ evolution under: output feedback (33) (a)–(c), heterogeneous feedback (37) (b)–(d). The horizontal scales under (a) and (b) denote the stiffness gain $\mathbf{K}_{\mathrm{s}}$ within different time periods.

RECBF constraint (42) is then inserted if $h^i \leq 4$ cm[14]. If QP is feasible then the CoM deceleration generated by (42) is achieved relying on feasible contact forces and consistent floating-base solution $\dot{\boldsymbol{v}}_{\mathrm{d}}$. In this experiment, $\hat{\boldsymbol{q}}_{\mathrm{d}}$ is the input command for the joint controllers.

For comparison purpose, three identical experimental scenarios have been conducted using the different closed-loop QP control schemes shown in Fig. 4:

- Experiment 1: feedforward ECBF constraint (31);
- Experiment 2: feedback ECBF constraint (36);
- Experiment 3: RECBF constraint (42).

The results are shown in Fig. 20. In the three experiments, K_{s}^h is computed as shown in [5] (Theorem 2). For Experiments 1 and 2, $K_{\mathrm{d}}^h = 2.4\sqrt{K_{\mathrm{s}}^h}$.

1) Experiment 1: see Fig. 20(a); the actual robot state $\boldsymbol{x}$ is not fed back to QP. We can see that $\mathbf{CoM}(\boldsymbol{x}_{\mathrm{d}})$ is within the limits and the set $\mathcal{C}_{\mathrm{d}}$ (22) is made forward invariant. However, since the robot is accounted for in the closed-loop system, forward invariance is not ensured for the set $\mathcal{C}$ (21). The mismatch between $\mathbf{CoM}(\boldsymbol{x}_{\mathrm{d}})$ and $\mathbf{CoM}(\boldsymbol{x})$ leads the latter to overshoot $X_{\max}$ limit with an amount of 2 cm, then to completely drift away from the polygon boundary at $t = 50$ s leading the robot to lose balance.

[14]The value of this threshold is conservative (user choice), but it can be decided by a high-level task scheduler or a task planner. In this experiment, we chose this value to confine the region within which the CoM acceleration is unconstrained. This helps to keep the CoM acceleration at low values.

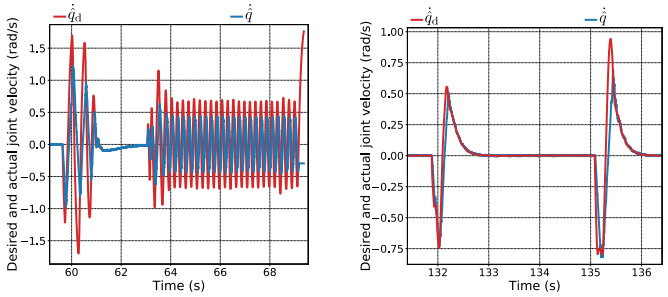

Fig. 16. Joint velocity tracking of the 2nd joint. (a) Closed-loop system under output feedback (33) at stiffness $\mathbf{K}_\mathrm{s} = 500\mathbf{I}$ leads to instability shown as fast oscillation of $\dot{\boldsymbol{q}}_\mathrm{d}$ tracked by $\dot{\boldsymbol{q}}$. (b) Closed-loop system under heterogeneous feedback (37) at stiffness $\mathbf{K}_\mathrm{s} = 800\mathbf{I}$ where $\dot{\boldsymbol{q}}_\mathrm{d}$ is kept bounded even though it is not well tracked by $\dot{\boldsymbol{q}}$, leading to a stable response.

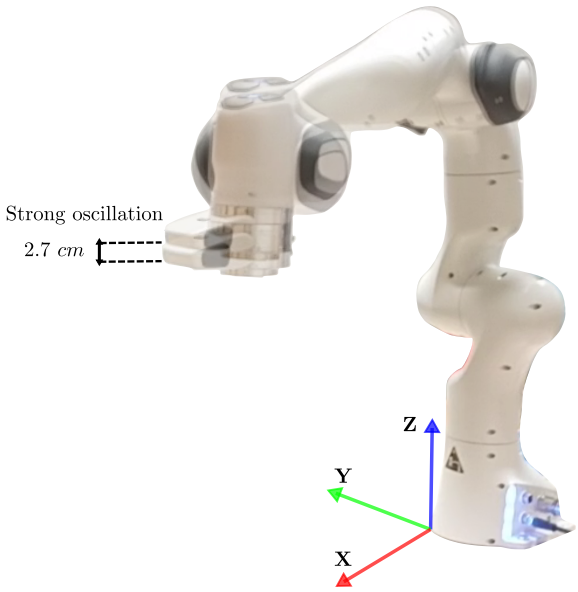

Fig. 17. Strong oscillations (highlighted in the yellow spot in Fig. 15(a)) due to non-robustness of output feedback control (33). The two superposed snapshots are taken with a time interval of $T = 133$ ms.

2) Experiment 2: see Fig. 20(b); the robot state is considered in closed-loop, but the ECBF formulation leads to instability. The bold dashed line shows the moment when ECBF constraint relative to X_max limit is inserted. Instantaneously, $\mathbf{CoM}(\boldsymbol{x}_\mathrm{d})$ velocity along X-axis starts to decrease (brown dash-dotted line). Nevertheless, $\mathbf{CoM}(\boldsymbol{x})$ velocity does not decrease immediately causing $\mathbf{CoM}(\boldsymbol{x})$ to keep moving toward X_max boundary. This lag is due to the underdamped flexibilities dynamics. In fact, the ECBF produced deceleration is mapped mainly by QP to the ankles joints through (30) as a little motion at these joints leads to a larger motion of the robot whole-body. However, the flexibilities underdamped dynamics leads $\mathbf{CoM}(\boldsymbol{x})$ to overshoot $\mathbf{CoM}(\boldsymbol{x}_\mathrm{d})$ and thereby the error $\boldsymbol{\eta}_\phi^h$ in (25) increases: at $t = 13$ s, $\mathbf{CoM}(\boldsymbol{x}_\mathrm{d})$ velocity is zero whereas $\mathbf{CoM}(\boldsymbol{x})$ is heading toward X_max boundary with a velocity of 0.10 m/s. Then at $t = 13.3$ s, $\mathbf{CoM}(\boldsymbol{x})$ velocity reaches zero while $\mathbf{CoM}(\boldsymbol{x}_\mathrm{d})$ is close to X_min boundary with a velocity of -0.16 m/s. When $\mathbf{CoM}(\boldsymbol{x})$ starts moving backward, its velocity increases highly leading to insert the ECBF constraint (relative to X_min boundary) with $\mathbf{CoM}(\boldsymbol{x})$ velocity reaching -0.22 m/s. At this point, the needed deceleration to stop $\mathbf{CoM}(\boldsymbol{x})$ at X_min boundary is high enough so that the QP fails to find corresponding feasible contact forces fulfilling (5), and the feet tip over.

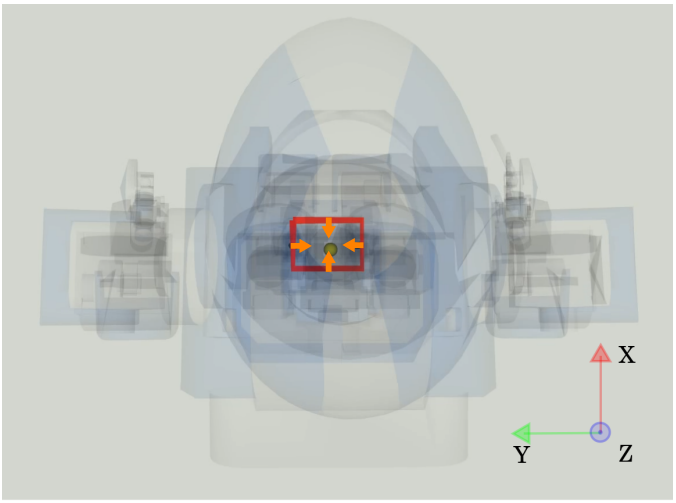

Fig. 18. Top-view of the humanoid robot HRP-4. The conservative equilibrium polygon is shown in red, the CoM in a yellow dot and the edges normal vectors in orange. The polygon is a rectangle in XY plane such that $X_\mathrm{max} = 5$ cm, $X_\mathrm{min} = -2$ cm, $Y_\mathrm{max} = 5$ cm, $Y_\mathrm{min} = -5$ cm.

Fig. 19. Rubber bushes (yellow) and dampers (orange) under HRP-4 ankles that induce non-modeled flexibilities.

3) Experiment 3: see Fig. 20(c); the constraint integral gain $K_\mathrm{i}^h = 8.4\sqrt{K_\mathrm{s}^h}$ and $K_\mathrm{d}^h = -1.2\sqrt{K_\mathrm{s}^h} < 0$. Note that Theorem 2 requirements are satisfied since $K_\mathrm{d}^h + K_\mathrm{i}^h > 0$ and thereby the eigenvalues of $\check{\mathbf{F}}_{\boldsymbol{\eta}_\mathrm{d}}$ in (70) are strictly negative. In particular, RECBF constraint (42) writes similarly to (38)

$$\mu^h \geq -7.2\sqrt{K_\mathrm{s}^h}\dot{h}_\mathrm{d} - 0.6\sqrt{K_\mathrm{s}^h}\left(\dot{h}_\mathrm{d} - \dot{h}\right) - K_\mathrm{s}^h h. \qquad (47)$$

The feedback term $(\dot{h}_\mathrm{d} - \dot{h})$ in (47) helps to withstand the flexibilities effect. In fact, Fig. 21 shows that, when (47) relative to X_max boundary is inserted, $\mathbf{CoM}(\boldsymbol{x}_\mathrm{d})$ velocity converges to zero while drifting toward $\mathbf{CoM}(\boldsymbol{x})$ velocity (X coordinates). Consequently, the delay between $\mathbf{CoM}(\boldsymbol{x}_\mathrm{d})$ and $\mathbf{CoM}(\boldsymbol{x})$ states is lowered. This compliance behavior is the key factor behind avoiding over-regulation that leads to excessive deceleration in Experiment 2. Also, compared to Experiment 1, $\mathbf{CoM}(\boldsymbol{x}_\mathrm{d})$ compensates for joint-dynamics static error allowing $\mathbf{CoM}(\boldsymbol{x})$ to converge asymptotically to the

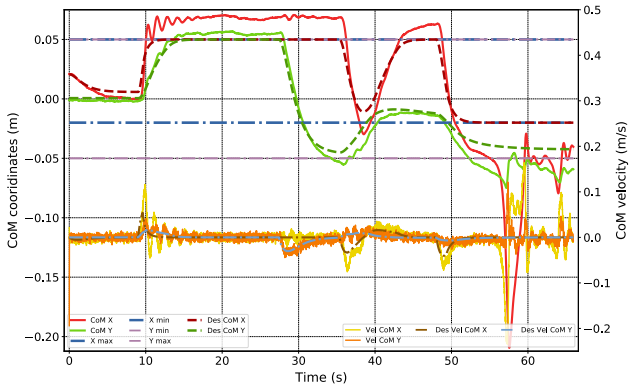

(a)

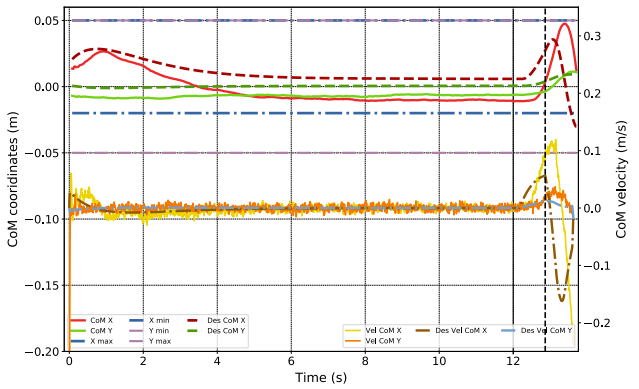

(b)

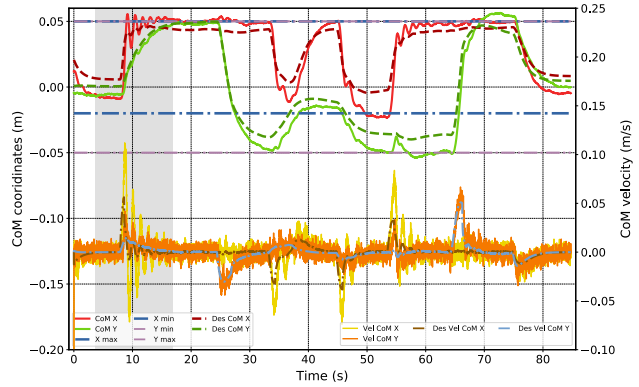

(c)

Fig. 20. Time Evolution of $\mathbf{CoM}(\boldsymbol{x})$, $\mathbf{CoM}(\boldsymbol{x}_{\mathrm{d}})$ and their respective velocities coordinates along X and Y axes. (a) Feedforward ECBF constraint (31). (b) Feedback ECBF constraint (36). (c) RECBF constraint (42). The gray time slot is zoomed-in in Fig. 21.

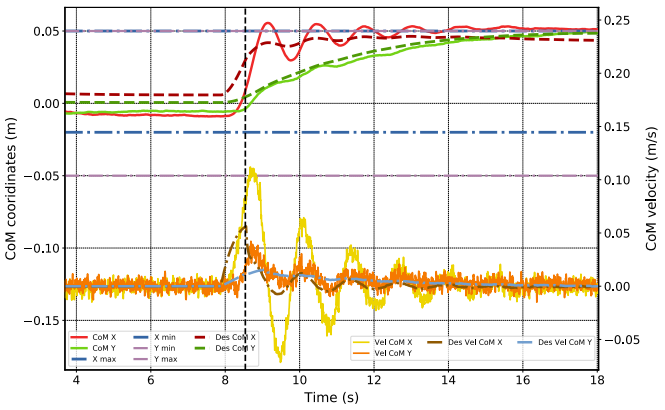

Fig. 21. Zoom-in of the gray time slot in Fig. 20(c). The bold dashed line denotes the moment when the RECBF constraint relative to $X_{\max}$ boundary is inserted in QP (43).

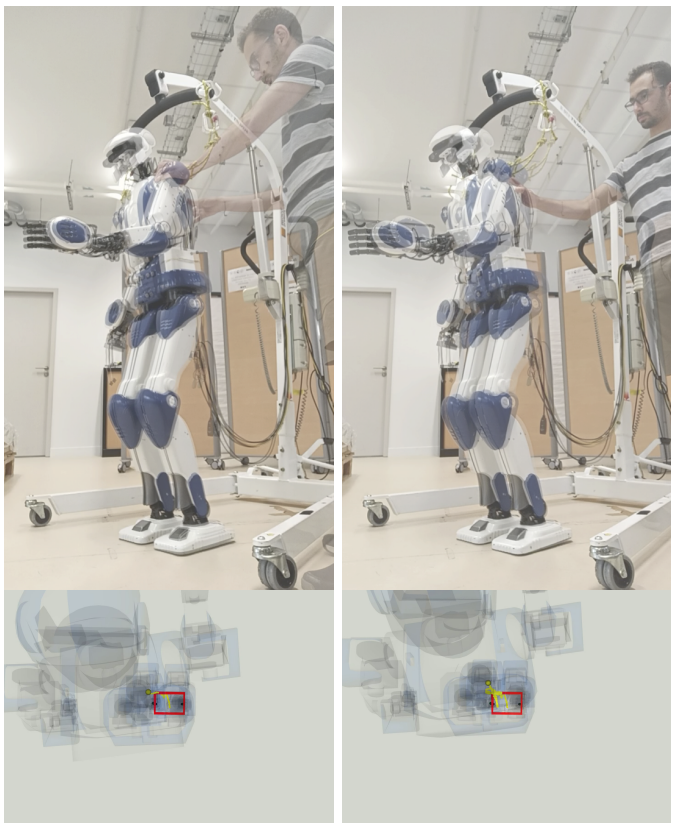

Fig. 22. Superposed snapshots of robust against pushing (experiment 4) in X (right-top) and Y (left-top) directions, with the corresponding top-view perspectives (bottom).

polygon boundaries. More related to Theorem 2, the set $\mathcal{C}_{\mathrm{d}}$ is made robustly stable, where the maximum overshoots along X and Y axes are: $X_{\max}^{\text{overshoot}} = 5.5$ mm, $X_{\min}^{\text{overshoot}} = 3.2$ mm, $Y_{\max}^{\text{overshoot}} = 6.5$ mm, $Y_{\min}^{\text{overshoot}} = 4$ mm.

4) Experiment 4: A fourth experiment is conducted to show the robust stability of $\mathcal{C}_{\mathrm{d}}$ against external pushes using the same RECBF constraint (47). Because of the high-stiffness joint controllers and high gear-ratio, the effect of the external disturbance forces is hardly observed at the joints' encoders. Yet, it can be measured by the floating-base observer affecting thereby the $\mathbf{CoM}(\boldsymbol{x})$ state.

First, a Cartesian target is defined for HRP-4 right hand such that $\mathbf{CoM}(\boldsymbol{x})$ reaches the polygon boundaries $X_{\max}$ and $Y_{\max}$. Then, the robot receives multiple external pushes from the operator (at the back and the shoulders) along X and Y axes (Fig. 22). Three persistent disturbance forces are applied, followed by two brief disturbances leading the flexibilities effect to enter into play (Fig. 23). During the whole experiment, $\mathbf{CoM}(\boldsymbol{x})$ is pushed away from the polygon boundaries with a distance of at least 2 cm. Here again, we can see the

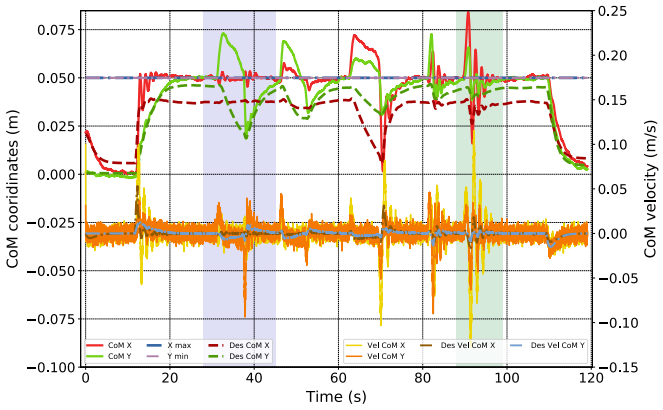

Fig. 23. Robustness of RECBF (42) against external pushes. The blue time slot denotes a persistent external push (Fig. 24(a)), and the green one denotes a brief external push (Fig. 24(b)).

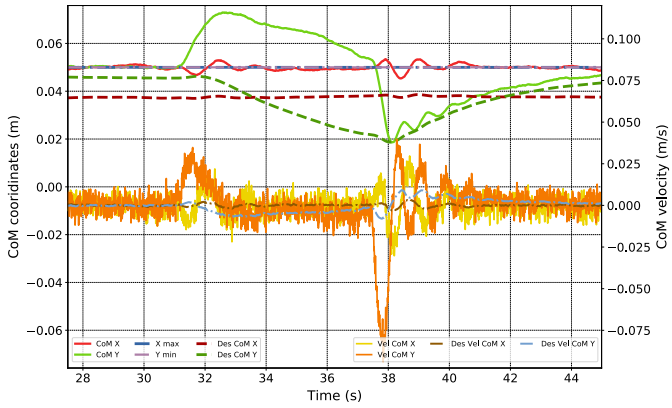

(a)

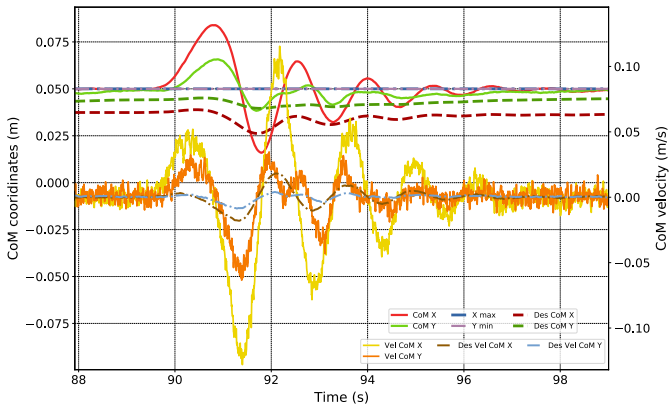

(b)

Fig. 24. (a) Zoom-in the blue time slot in Fig. 23 showing the response against a persistent push. (b) Zoom-in the green time slot in Fig. 23 showing the response against a brief push.

effect of the compliance feedback term. At the beginning of the persistent disturbance forces, $\mathbf{CoM}(\boldsymbol{x}_{\mathrm{d}})$ slightly complies with the disturbance. Then, when the compliance term is less predominant, the compliance is lost and QP generates solutions such that $\mathbf{CoM}(\boldsymbol{x}_{\mathrm{d}})$ counterbalances stiffly the disturbances enforcing $\mathbf{CoM}(\boldsymbol{x})$ to converge back smoothly to the polygon boundaries (Fig. 23(a)). When applying brief perturbations (Fig. 23(b)), $\mathbf{CoM}(\boldsymbol{x})$ converges asymptotically to the polygon boundaries while complying to the transient flexibility response. As in Experiment 3, the set $\mathcal{C}_{\mathrm{d}}$ is made robustly stable. Nevertheless and similarly to Section V-A, it goes at the expanse of K_{i}^{h} conservative tuning.

VI. Conclusion

In this paper, we propose a stable and robust closed-loop implementation of task-space QP control scheme for kinematic-controlled robots. Our solution allows free task-gains tuning and robust constraints design in the presence of non-modeled dynamics like joint-dynamics, flexibilities, and external disturbances. Our approach is proved to ensure the closed-loop stability by including integral feedback terms at both task and constraint levels leading to a robust convergence of their trajectories to the respective residual sets. Our method does not need the exact knowledge of the joint-dynamics model, but requires it to be ISS. Several experiments have been conducted on both floating-base and fixed-base robots to assess our new QP controller. Although not tackled in this paper, our approach can be extended to contact force control formulated as an admittance task [55]. Future works will focus on reducing the conservativeness on the choice of the integral feedback gains $\mathbf{K}_{\mathrm{i}}$ and K_{i}^{h}. Also, the conflict of RECBF with other constraints that leads to QP infeasibility is still an open problem. Up to now, constraints compatibility in QP control paradigms is among the main open questions that have not been well addressed and where model predictive control could be a candidate approach.

Appendix

A. Notations and Definitions

Bold small letters stand for vectors, bold capital letters for matrices, and normal letters for scalars. In this work, there are three classes of variables:

1) those with subscript $_{\mathrm{ref}}$ are the task-space reference targets given either by the operator or a task planner;
2) those with subscript $_{\mathrm{d}}$ are the desired variables in (i) the joint-space resulting from the integration of the desired acceleration (direct output of the QP), or (ii) in the task-space which are the mapping of the former; and
3) without any subscript are the variables tracking the desired once in 2)

– $\mathbb{R}$ and $\mathbb{R}^{+}$ are the sets of real and non-negative real numbers, respectively. For $\boldsymbol{\chi} \in \mathcal{X}$, $\boldsymbol{\alpha}_{\boldsymbol{\chi}}$ is the *velocity* of $\boldsymbol{\chi}$. If $\mathcal{X}$ is Euclidean then $\boldsymbol{\alpha}_{\boldsymbol{\chi}} = \dot{\boldsymbol{\chi}}$. $|\boldsymbol{\chi}|$ and $\|\boldsymbol{\chi}\|$ denote the component-wise absolute value and the Euclidean norm of $\boldsymbol{\chi}$, respectively. $\|\boldsymbol{\chi}\|_{\infty} = \sup_{t\geq 0} \|\boldsymbol{\chi}(t)\|$, $\boldsymbol{\chi} \in \mathbb{R}^{x}$ is said to be bounded if $\|\boldsymbol{\chi}\|_{\infty} < \infty$. The transpose of $\boldsymbol{\chi}$ is denoted $\boldsymbol{\chi}^{\mathsf{T}}$. $\underline{\lambda}(\mathbf{A}), \overline{\lambda}(\mathbf{A})$ denote respectively the minimum and maximum eigenvalues of matrix $\mathbf{A}$. All Jacobian matrices used in this work are assumed to be non-singular.

– $\gamma : \mathbb{R}^{+} \to \mathbb{R}^{+}$ is a class $\mathcal{K}_{\infty}$ function if it is continuous, strictly increasing, $\gamma(0) = 0$ and $\gamma(s) \xrightarrow{s\to\infty} \infty$.

– $\beta : \mathbb{R}^{+}\times\mathbb{R}^{+} \to \mathbb{R}^{+}$ is a class $\mathcal{KL}$ function if for each fixed $t \geq 0$, $\beta(s,t)$ is a class $\mathcal{K}$ function, and for each fixed $s \geq 0$, it decreases to 0 as $t \to \infty$.

$\| \ \|_\Omega$ denotes the Euclidean point-to-set distance: $\|\boldsymbol{\chi}\|_\Omega = \mathrm{dist}(\boldsymbol{\chi};\Omega) = \inf\{\mathrm{dist}(\boldsymbol{\chi},\boldsymbol{a}) | \boldsymbol{a}\in\Omega\} = \inf_{\boldsymbol{a}\in\Omega} \|\boldsymbol{\chi}-\boldsymbol{a}\|$.

– Let us consider the system

$$\dot{\boldsymbol{\chi}} = f_{\boldsymbol{\chi}}(\boldsymbol{\chi}, \boldsymbol{\upsilon}), \tag{48}$$

where $\boldsymbol{\chi} \in \mathbb{R}^x$ and $\boldsymbol{\upsilon} \in \mathbb{R}^u$. For any initial condition $\boldsymbol{\chi}(t_0) \in \mathbb{R}^x$, there exists a maximum time interval $I(\boldsymbol{\chi}(t_0)) = [t_0, t_{\max}]$ such that $\boldsymbol{\chi}(t)$ is the unique solution of (48) on $I(\boldsymbol{\chi}(t_0))$. If $t_{\max} = \infty$ then $f_{\boldsymbol{\chi}(t_0)}$ is forward complete. System (48) is said to be *autonomous* when $\boldsymbol{\upsilon} = 0$. A set $\mathcal{S} \subset \mathbb{R}^x$ is called *forward invariant* w.r.t autonomous system (48) if $\forall \boldsymbol{\chi}(t_0) \in \mathcal{S}$ then $\boldsymbol{\chi}(t) \in \mathcal{S}$, $\forall t \in I(\boldsymbol{\chi}(t_0))$. In addition, a closed and forward invariant set $\mathcal{S} \subset \mathbb{R}^x$ is asymptotically stable for a forward-complete autonomous system (48) if there exist on open set $\mathcal{R} \supseteq \mathcal{S}$, and a class $\mathcal{KL}$ function β such that

$$\|\boldsymbol{\chi}(t)\|_{\mathcal{S}} \leq \beta\left(\|\boldsymbol{\chi}(t_0)\|_{\mathcal{S}}, t - t_0\right), \ \forall \boldsymbol{\chi}(t_0) \in \mathcal{R}.$$

– **Robust Global Uniform Asymptotic Stability:** [56], [57] Consider the system

$$\dot{\boldsymbol{\chi}} = f_{\boldsymbol{\chi}}(\boldsymbol{\chi}, \boldsymbol{\upsilon}, t). \tag{49}$$

Fix a control $\boldsymbol{\upsilon}$, and let $\Omega \subset \mathcal{X}$ be a compact set containing the origin. The solutions of the system (49) are Robustly Globally Uniformly Asymptotically Stable w.r.t Ω (RGUAS-Ω) when there exists class $\mathcal{KL}$ function β such that for all admissible measurements, admissible disturbance, and initial conditions $(\boldsymbol{\chi}(t_0), t_0) \in \mathcal{X} \times \mathbb{R}$, all solutions $\boldsymbol{\chi}(t)$ exist and satisfy

$$\|\boldsymbol{\chi}(t)\|_\Omega \leq \beta(\|\boldsymbol{\chi}(t_0)\|_\Omega, t - t_0). \tag{50}$$

System (49) is **robustly practically stabilizable** when $\forall \epsilon > 0$ there exist an admissible control and a compact set $\Omega \subset \mathcal{X}$ satisfying $0 \in \Omega \subset \epsilon\mathcal{B}$, with $\mathcal{B}$ the unit ball set, such that the solutions $\boldsymbol{\chi}(t)$ are RGUAS-Ω.

– **Rayleight-Ritz Inequality**: [58] Given a symmetric matrix $\mathbf{A} \in \mathbb{R}^{x\times x}$ the following inequality holds $\forall \boldsymbol{\chi} \in \mathbb{R}^x$:

$$\underline{\lambda}(\mathbf{A}) \|\boldsymbol{\chi}\|^2 \leq \boldsymbol{\chi}^\mathsf{T}\mathbf{A}\chi \leq \overline{\lambda}(\mathbf{A}) \|\boldsymbol{\chi}\|^2. \tag{51}$$

– **Schwartz inequality**: [59] $\forall \boldsymbol{\chi}, \boldsymbol{\zeta} \in \mathbb{R}^x$,

$$|\boldsymbol{\chi}^\mathsf{T}\boldsymbol{\zeta}| \leq \|\boldsymbol{\chi}\| \|\boldsymbol{\zeta}\|. \tag{52}$$

B. Proof of Proposition 1

Proof. The proof is established for $\boldsymbol{\eta}_\mathrm{d}$, the same steps apply for $\boldsymbol{\eta}_\mathrm{d}^h$. Here, the dependency on time (t) is made explicit. Given (17), let us assume $\exists \boldsymbol{\mu} \in \mathbb{R}^m \mid \boldsymbol{\eta}_\mathrm{d}(t)$ is bounded

$$\begin{aligned} \|\boldsymbol{\eta}_\mathrm{d}(t)\| \leq M \Rightarrow \begin{cases} \|\boldsymbol{e}_\mathbf{d}(t)\| \leq M \\ \|\dot{\boldsymbol{e}}_\mathbf{d}(t)\| \leq M \end{cases}, \forall t \geq 0, \\ (13) \Leftrightarrow \begin{cases} \|\boldsymbol{s}(\boldsymbol{q}_\mathrm{d}(t)) - \boldsymbol{s}_\mathrm{ref}(t)\| \leq M, \\ \|\mathbf{J}_\mathrm{d}\boldsymbol{\alpha}_{\boldsymbol{q}_\mathrm{d}}(t) - \dot{\boldsymbol{s}}_\mathrm{ref}(t)\| \leq M, \end{cases} \end{aligned} \tag{53}$$

where $\boldsymbol{s}_\mathrm{ref}(t)$ and $\dot{\boldsymbol{s}}_\mathrm{ref}(t)$ are obviously bounded. Let us prove that if $\boldsymbol{e}_\mathbf{d}(t)$ is bounded then $\boldsymbol{q}_\mathrm{d}(t)$ is bounded. Let us define $\boldsymbol{q}_\mathrm{ref}(t) \in \mathcal{Q}$[15] with

$$\mathcal{Q} = \left\{\boldsymbol{q}_\mathrm{d}(t) \in \mathbb{R}^{7+n} : \boldsymbol{s}\left(\boldsymbol{q}_\mathrm{d}(t)\right) = \boldsymbol{s}_\mathrm{ref}(t)\right\}. \tag{54}$$

[15]In (54), $\boldsymbol{s}_\mathrm{ref}$ is assumed to be strictly reachable. Otherwise, we can define $\mathcal{Q}$ as $\mathcal{Q} = \left\{\boldsymbol{q}_\mathrm{d}^*(t) \in \mathbb{R}^{7+n} : \boldsymbol{q}_\mathrm{d}^* = \arg\min \left\|\boldsymbol{s}\left(\boldsymbol{q}_\mathrm{d}(t)\right) - \boldsymbol{s}_\mathrm{ref}(t)\right\|\right\}$ which leads to $\boldsymbol{s}\left(\boldsymbol{q}_\mathrm{ref}(t)\right) = \boldsymbol{s}_\mathrm{ref}(t) + \boldsymbol{\delta}_\boldsymbol{s}(t)$, with $\boldsymbol{\delta}_\boldsymbol{s}(t) \in \mathbb{R}^m$ bounded. The remaining of the proof is not affected.

Thus, by putting $\Delta\boldsymbol{q}_\mathrm{d}(t) = \boldsymbol{q}_\mathrm{d}(t) - \boldsymbol{q}_\mathrm{ref}(t)$, $\boldsymbol{s}\left(\boldsymbol{q}_\mathrm{d}(t)\right)$ writes using Taylor expansion

$$\begin{aligned} \boldsymbol{s}\left(\boldsymbol{q}_\mathrm{d}(t)\right) &= \boldsymbol{s}\left(\boldsymbol{q}_\mathrm{ref}(t) + \Delta\boldsymbol{q}_\mathrm{d}(t)\right), \\ &= \boldsymbol{s}_\mathrm{ref}(t) + R(\Delta\boldsymbol{q}_\mathrm{d}(t)), \\ R(\Delta\boldsymbol{q}_\mathrm{d}(t)) &= \left.\frac{\partial \boldsymbol{s}(\boldsymbol{q}_\mathrm{d}(t))}{\partial \boldsymbol{q}_\mathrm{d}(t)}\right|_{\boldsymbol{q}_\mathrm{d}(t)=\check{\boldsymbol{q}}_\mathrm{d}(t)} \Delta\boldsymbol{q}_\mathrm{d}(t), \end{aligned} \tag{55}$$

where $R(\Delta\boldsymbol{q}_\mathrm{d}(t))$ is the Lagrange remainder with $\check{\boldsymbol{q}}_\mathrm{d}(t) = \boldsymbol{q}_\mathrm{ref}(t) + \theta\Delta\boldsymbol{q}_\mathrm{d}(t)$, $0 \leq \theta \leq 1$ [60, Chapter IV, Section 6]. From (53), (55) we have

$$\left\|R\left(\Delta\boldsymbol{q}_\mathrm{d}(t)\right)\right\| \leq M. \tag{56}$$

If $\frac{\partial \boldsymbol{s}(\boldsymbol{q}_\mathrm{d}(t))}{\partial \boldsymbol{q}_\mathrm{d}(t)}$ is non-singular, then $\forall\theta$ with $0 \leq \theta \leq 1$ there exist b, b_0, $b \geq b_0 > 0$ such that [61]

$$\begin{aligned} &\left\|R\left(\Delta\boldsymbol{q}_\mathrm{d}(t)\right)\right\| = b\left\|\Delta\boldsymbol{q}_\mathrm{d}(t)\right\| \Rightarrow \left\|\Delta\boldsymbol{q}_\mathrm{d}(t)\right\| \leq \frac{M}{b}, \\ &\Leftrightarrow \left\|\boldsymbol{q}_\mathrm{d}(t)\right\| - \left\|\boldsymbol{q}_\mathrm{ref}(t)\right\| \leq \left\|\Delta\boldsymbol{q}_\mathrm{d}(t)\right\| \leq \frac{M}{b}, \\ &\Rightarrow \left\|\boldsymbol{q}_\mathrm{d}(t)\right\| \leq \frac{M}{b} + \left\|\boldsymbol{q}_\mathrm{ref}(t)\right\|. \end{aligned} \tag{57}$$

Given that $\boldsymbol{q}_\mathrm{ref}(t)$ is bounded, then $\boldsymbol{q}_\mathrm{d}(t)$ is bounded.

Now, let us prove that if $\dot{\boldsymbol{e}}_\mathbf{d}(t)$ is bounded then $\boldsymbol{\alpha}_{\boldsymbol{q}_\mathrm{d}}(t)$ is bounded. $\boldsymbol{\alpha}_{\boldsymbol{q}_\mathrm{d}}(t)$ can be written as $\boldsymbol{\alpha}_{\boldsymbol{q}_\mathrm{d}}(t) = \hat{\boldsymbol{\alpha}}_{\boldsymbol{q}_\mathrm{d}}(t) + \boldsymbol{\alpha}^\#_{\boldsymbol{q}_\mathrm{d}}(t)$ such that $\boldsymbol{\alpha}^\#_{\boldsymbol{q}_\mathrm{d}}(t) \in \ker\{\mathbf{J}_\mathrm{d}\}$ with $\boldsymbol{\alpha}^\#_{\boldsymbol{q}_\mathrm{d}}(t) = \left(\mathbf{I} - {\mathbf{J}_\mathrm{d}}^+\mathbf{J}_\mathrm{d}\right)\boldsymbol{\nu}(t)$, where ${\mathbf{J}_\mathrm{d}}^+$ is the Moore-Penrose Jacobian inverse and $\boldsymbol{\nu}(t) \in \mathbb{R}^{6+n}$ denotes the remaining velocity redundancy. In QP (43), the redundancy state is bounded by a secondary (posture) task. Furthermore, (5) and (43d) ensures bounded and feasible floating base solutions. Hence, $\boldsymbol{\nu}(t)$ is bounded. Let us show the boundedness of $\hat{\boldsymbol{\alpha}}_{\boldsymbol{q}_\mathrm{d}}(t)$. From (53)

$$\begin{aligned} \left\|\mathbf{J}_\mathrm{d}\hat{\boldsymbol{\alpha}}_{\boldsymbol{q}_\mathrm{d}}(t)\right\| - \left\|\dot{\boldsymbol{s}}_\mathrm{ref}(t)\right\| \leq \left\|\mathbf{J}_\mathrm{d}\hat{\boldsymbol{\alpha}}_{\boldsymbol{q}_\mathrm{d}}(t) - \dot{\boldsymbol{s}}_\mathrm{ref}(t)\right\| \leq M, \\ \Rightarrow \left\|\mathbf{J}_\mathrm{d}\hat{\boldsymbol{\alpha}}_{\boldsymbol{q}_\mathrm{d}}(t)\right\| \leq M + \left\|\dot{\boldsymbol{s}}_\mathrm{ref}(t)\right\|. \end{aligned} \tag{58}$$

Given that $\mathbf{J}_\mathrm{d}$ is non-singular, then there exist b', b'_0 with $b' \geq b'_0 > 0$ such that [61]

$$\begin{aligned} \left\|\mathbf{J}_\mathrm{d}\hat{\boldsymbol{\alpha}}_{\boldsymbol{q}_\mathrm{d}}(t)\right\| = b'\left\|\hat{\boldsymbol{\alpha}}_{\boldsymbol{q}_\mathrm{d}}(t)\right\| \leq M + \left\|\dot{\boldsymbol{s}}_\mathrm{ref}(t)\right\|, \\ \Rightarrow \left\|\hat{\boldsymbol{\alpha}}_{\boldsymbol{q}_\mathrm{d}}(t)\right\| \leq \frac{M + \left\|\dot{\boldsymbol{s}}_\mathrm{ref}(t)\right\|}{b'}. \end{aligned} \tag{59}$$

Hence, $\boldsymbol{\alpha}_{\boldsymbol{q}_\mathrm{d}}(t)$ is bounded such that

$$\left\|\boldsymbol{\alpha}_{\boldsymbol{q}_\mathrm{d}}(t)\right\| \leq \left\|\hat{\boldsymbol{\alpha}}_{\boldsymbol{q}_\mathrm{d}}(t)\right\| + \left\|\mathbf{I} - {\mathbf{J}_\mathrm{d}}^+\mathbf{J}_\mathrm{d}\right\| \left\|\boldsymbol{\nu}(t)\right\|. \tag{60}$$

From (6) and following from (60) and (57) $\boldsymbol{x}_\mathrm{d}(t)$ is bounded implying that, given (19), $\exists \dot{\boldsymbol{\alpha}}_{\boldsymbol{q}_\mathrm{d}} \in \mathcal{U}$ such that $\boldsymbol{x}_\mathrm{d}(t)$ is bounded. □

C. Proof of Proposition 2

Proof. As in Proposition 1 proof, Proposition 2 proof is established for $\boldsymbol{\eta}_\mathrm{d}$ (the same steps apply for $\boldsymbol{\eta}_\mathrm{d}^h$) and the dependency on time (t) is made explicit. Let us consider system (17) and assume that there exists $\boldsymbol{\mu}$ such that $\boldsymbol{\eta}_\mathrm{d}(t)$ is (uniformly) ultimately bounded. Then, there exists an ultimate bound $\varrho_{\boldsymbol{\eta}_\mathrm{d}} > 0$, such that $\forall M_{\boldsymbol{\eta}_\mathrm{d}} > 0$, $\exists T_{\boldsymbol{\eta}_\mathrm{d}} = T_{\boldsymbol{\eta}_\mathrm{d}}(M_{\boldsymbol{\eta}_\mathrm{d}}, \varrho_{\boldsymbol{\eta}_\mathrm{d}}) > 0$ such that [49, Definition 4.6]

$$\left\|\boldsymbol{\eta}_\mathrm{d}(t_0)\right\| \leq M_{\boldsymbol{\eta}_\mathrm{d}} \Rightarrow \left\|\boldsymbol{\eta}_\mathrm{d}(t)\right\| \leq \varrho_{\boldsymbol{\eta}_\mathrm{d}}, \ \forall t \geq t_0 + T_{\boldsymbol{\eta}_\mathrm{d}}. \tag{61}$$

From Proposition 1 proof in Appendix B and (61), it yields that there exists $\varrho_{\hat{\boldsymbol{x}}_\mathrm{d}} = \varrho_{\hat{\boldsymbol{x}}_\mathrm{d}}(\varrho_{\boldsymbol{\eta}_\mathrm{d}}) > 0$ such that $\left\|\hat{\boldsymbol{x}}_\mathrm{d}(t)\right\| \leq \varrho_{\hat{\boldsymbol{x}}_\mathrm{d}},\ \forall t \geq t_0 + T_{\boldsymbol{\eta}_\mathrm{d}}$. Hence, from Assumption 1, we get

$$\begin{aligned}\left\|\hat{\boldsymbol{\phi}}(t)\right\| &= \left\|\hat{\boldsymbol{x}}(t) - \hat{\boldsymbol{x}}_\mathrm{d}(t)\right\| \leq \sigma \\ &\Rightarrow \left\|\hat{\boldsymbol{x}}(t)\right\| \leq \sigma + \left\|\hat{\boldsymbol{x}}_\mathrm{d}(t)\right\| \leq \sigma + \varrho_{\hat{\boldsymbol{x}}_\mathrm{d}},\ \forall t \geq t_0 + T_{\boldsymbol{\eta}_\mathrm{d}}.\end{aligned}$$

In addition, the robot floating-base state $\boldsymbol{x}^{\mathrm{FB}}(t)$ is bounded by assumption which leads to the boundedness of $\boldsymbol{x}$ (6). Thus, from (15) and (61), there exists an ultimate bound $\varrho_{\boldsymbol{\eta}} = \varrho_{\boldsymbol{\eta}_\mathrm{d}} + \left\|\boldsymbol{\eta}_{\boldsymbol{\phi}}\right\|_\infty > 0$, such that $\forall M_{\boldsymbol{\eta}} = M_{\boldsymbol{\eta}_\mathrm{d}} + \left\|\boldsymbol{\eta}_{\boldsymbol{\phi}}(t_0)\right\| > 0$, there exists $T_{\boldsymbol{\eta}} = T_{\boldsymbol{\eta}}(M_{\boldsymbol{\eta}}, \varrho_{\boldsymbol{\eta}}) > 0$ such that

$$\left\|\boldsymbol{\eta}(t_0)\right\| \leq M_{\boldsymbol{\eta}} \Rightarrow \left\|\boldsymbol{\eta}(t)\right\| \leq \varrho_{\boldsymbol{\eta}},\ \forall t \geq t_0 + T_{\boldsymbol{\eta}}, \tag{62}$$

which yields to $\boldsymbol{\eta}(t)$ is (uniformly) ultimately bounded. □

D. Proof of Theorem 1

Proof. Replacing (37) in (17) yields to

$$\dot{\boldsymbol{\eta}}_\mathrm{d} = \check{\mathbf{F}}_{\boldsymbol{\eta}_\mathrm{d}} \boldsymbol{\eta}_\mathrm{d} - \mathbf{B}_{\boldsymbol{\eta}_\mathrm{d}} \mathbf{K} \boldsymbol{\eta}_{\boldsymbol{\phi}}, \tag{63}$$

where $\check{\mathbf{F}}_{\boldsymbol{\eta}_\mathrm{d}}$ and $\mathbf{K}$ are defined as in Theorem 1 and (33), respectively. Let us consider the following Lyapunov function associated to (63)

$$\gamma_1\left(\left\|\boldsymbol{\eta}_\mathrm{d}\right\|\right) \leq V(\boldsymbol{\eta}_\mathrm{d}) = \frac{1}{2}\boldsymbol{\eta}_\mathrm{d}{}^\mathsf{T} \mathbf{P}_{\boldsymbol{\eta}_\mathrm{d}} \boldsymbol{\eta}_\mathrm{d} \leq \gamma_2\left(\left\|\boldsymbol{\eta}_\mathrm{d}\right\|\right) \tag{64}$$

where $\gamma_1\left(\left\|\boldsymbol{\eta}_\mathrm{d}\right\|\right) = \frac{\underline{\lambda}(\mathbf{P}_{\boldsymbol{\eta}_\mathrm{d}})}{2}\left\|\boldsymbol{\eta}_\mathrm{d}\right\|^2$ and $\gamma_2\left(\left\|\boldsymbol{\eta}_\mathrm{d}\right\|\right) = \frac{\overline{\lambda}(\mathbf{P}_{\boldsymbol{\eta}_\mathrm{d}})}{2}\left\|\boldsymbol{\eta}_\mathrm{d}\right\|^2$ are class $\mathcal{K}_\infty$ functions, and $\mathbf{P}_{\boldsymbol{\eta}_\mathrm{d}} = \mathbf{P}_{\boldsymbol{\eta}_\mathrm{d}}^\mathsf{T} > 0$ is the solution of the following Algebraic Riccati Equation (ARE)

$$\check{\mathbf{F}}_{\boldsymbol{\eta}_\mathrm{d}}^\mathsf{T} \mathbf{P}_{\boldsymbol{\eta}_\mathrm{d}} + \mathbf{P}_{\boldsymbol{\eta}_\mathrm{d}} \check{\mathbf{F}}_{\boldsymbol{\eta}_\mathrm{d}} = -\mathbf{Q}_{\boldsymbol{\eta}_\mathrm{d}} = -\begin{bmatrix}\mathbf{K}_\mathrm{i} & 0\\ 0 & \mathbf{K}_\mathrm{i}\end{bmatrix}. \tag{65}$$

Given (65), $\dot{V} = -\frac{1}{2}\boldsymbol{\eta}_\mathrm{d}{}^\mathsf{T}\mathbf{Q}_{\boldsymbol{\eta}_\mathrm{d}}\boldsymbol{\eta}_\mathrm{d} - \boldsymbol{\eta}_\mathrm{d}{}^\mathsf{T}\mathbf{P}_{\boldsymbol{\eta}_\mathrm{d}}\mathbf{B}_{\boldsymbol{\eta}_\mathrm{d}}\mathbf{K}\boldsymbol{\eta}_{\boldsymbol{\phi}}$. Given that $\left\|\mathbf{B}_{\boldsymbol{\eta}_\mathrm{d}}\right\| = 1$, $\left\|\mathbf{P}_{\boldsymbol{\eta}_\mathrm{d}}\right\| = \overline{\lambda}(\mathbf{P}_{\boldsymbol{\eta}_\mathrm{d}})$ and $\underline{\lambda}(\mathbf{Q}_{\boldsymbol{\eta}_\mathrm{d}}) = \underline{\lambda}(\mathbf{K}_\mathrm{i}) > 0$, and using Rayleight-Ritz (51) and Schwartz (52) inequalities, $\dot{V}$ is bounded such that

$$\begin{aligned}\dot{V} \leq &-\frac{1-\vartheta}{2}\underline{\lambda}(\mathbf{K}_\mathrm{i})\left\|\boldsymbol{\eta}_\mathrm{d}\right\|^2 \\ &-\frac{\vartheta}{2}\underline{\lambda}(\mathbf{K}_\mathrm{i})\left\|\boldsymbol{\eta}_\mathrm{d}\right\|\left(\left\|\boldsymbol{\eta}_\mathrm{d}\right\| - \frac{2\overline{\lambda}(\mathbf{P}_{\boldsymbol{\eta}_\mathrm{d}})\left\|\mathbf{K}\right\|\left\|\boldsymbol{\eta}_{\boldsymbol{\phi}}\right\|}{\vartheta\underline{\lambda}(\mathbf{K}_\mathrm{i})}\right),\end{aligned} \tag{66}$$

with $0 < \vartheta < 1$. Thus, if $\mathbf{K}_\mathrm{i}$ is chosen such that

$$\left\|\boldsymbol{\eta}_\mathrm{d}\right\| \geq \frac{2\overline{\lambda}(\mathbf{P}_{\boldsymbol{\eta}_\mathrm{d}})\left\|K\right\|}{\vartheta\underline{\lambda}(\mathbf{K}_\mathrm{i})}\left\|\boldsymbol{\eta}_{\boldsymbol{\phi}}\right\|_\infty, \tag{67}$$

then $\dot{V} \leq -\frac{1-\vartheta}{2}\underline{\lambda}(\mathbf{K}_\mathrm{i})\left\|\boldsymbol{\eta}_\mathrm{d}\right\|^2$. By the virtue of [49, Theorem 4.18], $\boldsymbol{\eta}_\mathrm{d}$ is uniformly ultimately bounded with ultimate bound $\varrho = \sqrt{\frac{\overline{\lambda}(\mathbf{P}_{\boldsymbol{\eta}_\mathrm{d}})}{\underline{\lambda}(\mathbf{P}_{\boldsymbol{\eta}_\mathrm{d}})}}\frac{2\overline{\lambda}(\mathbf{P}_{\boldsymbol{\eta}_\mathrm{d}})\left\|\mathbf{K}\right\|}{\vartheta\underline{\lambda}(\mathbf{K}_\mathrm{i})}\left\|\boldsymbol{\eta}_{\boldsymbol{\phi}}\right\|_\infty$. Furthermore, $\forall \left\|\boldsymbol{\eta}_\mathrm{d}(t_0)\right\| \leq M$ there exist $T = T(M, \varrho) > 0$, a class $\mathcal{KL}$ function β, and a closed set $\Omega_{\boldsymbol{\eta}_\mathrm{d}} = \left\{\boldsymbol{\eta}_\mathrm{d} \in H : \left\|\boldsymbol{\eta}_\mathrm{d}\right\| \leq \varrho\right\}$ such that

$$\begin{aligned}&\left\|\boldsymbol{\eta}_\mathrm{d}(t)\right\|_{\Omega_{\boldsymbol{\eta}_\mathrm{d}}} \leq \beta\left(\left\|\boldsymbol{\eta}_\mathrm{d}(t_0)\right\|_{\Omega_{\boldsymbol{\eta}_\mathrm{d}}}, t - t_0\right),\ \forall t_0 \leq t \leq t_0 + T, \\ &\left\|\boldsymbol{\eta}_\mathrm{d}(t)\right\|_{\Omega_{\boldsymbol{\eta}_\mathrm{d}}} = 0,\ \forall t \leq t_0 + T.\end{aligned} \tag{68}$$

Given (67), the residual set $\Omega_{\boldsymbol{\eta}_\mathrm{d}}$ can be made arbitrarily small by $\mathbf{K}_\mathrm{i}$. Hence, $\boldsymbol{\eta}_\mathrm{d}$ is robustly practically stable w.r.t $\Omega_{\boldsymbol{\eta}_\mathrm{d}}$ [57, Defintion 3.2]. □

E. Proof of Theorem 2

Proof. The matrix gain $\check{\mathbf{K}}^h$ is chosen to ensure that h_d is ECBF for the nominal system $\boldsymbol{\eta}_{\boldsymbol{\phi}}^h = \mathbf{0}$.

Now, let us prove that $\boldsymbol{\eta}_\mathrm{d}^h$ is uniformly ultimately bounded. Inequality (42) can be expressed as

$$\mu^h = -\mathbf{L}^h\boldsymbol{\psi}^h + \delta^h(t),\ 0 \leq \delta^h(t) \leq \delta^h_{\max}, \tag{69}$$

with $\delta^h(t)$ a slack variable that facilitates the manipulation of (42). Given (69), system (27) becomes

$$\dot{\boldsymbol{\eta}}_\mathbf{d}^{\boldsymbol{h}} = \check{\mathbf{F}}_{\boldsymbol{\eta}_\mathrm{d}^h}\boldsymbol{\eta}_\mathrm{d}^h + \mathbf{B}_{\boldsymbol{\eta}_\mathrm{d}^h}\left(-\mathbf{K}^h\boldsymbol{\eta}_{\boldsymbol{\phi}}^h + \delta^h(t)\right), \tag{70}$$

where $\mathbf{K}^h$ defined as in (36), and $\check{\mathbf{F}}_{\boldsymbol{\eta}_\mathrm{d}^h} = \mathbf{A}_{\boldsymbol{\eta}_\mathrm{d}^h} - \mathbf{B}_{\boldsymbol{\eta}_\mathrm{d}^h}\check{\mathbf{K}}^h$. Let us consider the following Lyapunov function [47][16]

$$V = \begin{cases} 0, \text{ if } \boldsymbol{x}_\mathrm{d} \in \mathcal{C}_\mathrm{d} \\ \frac{1}{2}\boldsymbol{\eta}_\mathrm{d}^h{}^\mathsf{T}\mathbf{P}_{\boldsymbol{\eta}_\mathrm{d}^h}\boldsymbol{\eta}_\mathrm{d}^h, \text{ otherwise}\end{cases} \tag{71}$$

where $\mathbf{P}_{\boldsymbol{\eta}_\mathrm{d}^h} = \mathbf{P}_{\boldsymbol{\eta}_\mathrm{d}^h}^\mathsf{T} > 0$ is the solution of the following ARE

$$\check{\mathbf{F}}_{\boldsymbol{\eta}_\mathrm{d}^h}^\mathsf{T}\mathbf{P}_{\boldsymbol{\eta}_\mathrm{d}^h} + \mathbf{P}_{\boldsymbol{\eta}_\mathrm{d}^h}\check{\mathbf{F}}_{\boldsymbol{\eta}_\mathrm{d}^h} = -\mathbf{Q}_{\boldsymbol{\eta}_\mathrm{d}^h} = -\begin{bmatrix}K_\mathrm{i}^h & 0\\ 0 & K_\mathrm{i}^h\end{bmatrix}. \tag{72}$$

The goal is to show that there exists a set $\mathcal{C}_{\mathrm{d}\sigma} \supseteq \mathcal{C}_\mathrm{d}$ such that $\dot{V} < 0, \forall \boldsymbol{x}_\mathrm{d} \in \mathbb{R}^{13+2n} \setminus \mathcal{C}_{\mathrm{d}\sigma}$. Using (72), $\dot{V}$ is computed as

$$\dot{V} = -\frac{1}{2}\boldsymbol{\eta}_\mathrm{d}^h{}^\mathsf{T}\mathbf{Q}_{\boldsymbol{\eta}_\mathrm{d}^h}\boldsymbol{\eta}_\mathrm{d}^h + \boldsymbol{\eta}_\mathrm{d}^h{}^\mathsf{T}\mathbf{P}_{\boldsymbol{\eta}_\mathrm{d}^h}\mathbf{B}_{\boldsymbol{\eta}_\mathrm{d}^h}\left(-\mathbf{K}^h\boldsymbol{\eta}_{\boldsymbol{\phi}}^h + \delta^h(t)\right). \tag{73}$$

Using Rayleight-Ritz (51) and Schwartz (52) inequalities, (73) becomes

$$\begin{aligned}\dot{V} \leq &-\frac{1}{2}\underline{\lambda}(\mathbf{Q}_{\boldsymbol{\eta}_\mathrm{d}^h})\left\|\boldsymbol{\eta}_\mathrm{d}^h\right\|^2 \\ &+ \left\|\boldsymbol{\eta}_\mathrm{d}^h\right\|\left\|\mathbf{P}_{\boldsymbol{\eta}_\mathrm{d}^h}\right\|\left\|\mathbf{B}_{\boldsymbol{\eta}_\mathrm{d}^h}\right\|\left(\left\|\mathbf{K}^h\right\|\left\|\boldsymbol{\eta}_{\boldsymbol{\phi}}^h\right\| + \left\|\delta^h(t)\right\|\right).\end{aligned} \tag{74}$$

By putting $\varphi = \left\|\mathbf{K}^h\right\|\left\|\boldsymbol{\eta}_{\boldsymbol{\phi}}^h\right\| + \left\|\delta^h(t)\right\|$, and given that $\underline{\lambda}(\mathbf{Q}_{\boldsymbol{\eta}_\mathrm{d}^h}) = K_\mathrm{i}^h > 0$, $\left\|\mathbf{P}_{\boldsymbol{\eta}_\mathrm{d}^h}\right\| = \overline{\lambda}(\mathbf{P}_{\boldsymbol{\eta}_\mathrm{d}^h})$, $\left\|\mathbf{B}_{\boldsymbol{\eta}_\mathrm{d}^h}\right\| = 1$, then

$$\begin{aligned}\dot{V} \leq &-\frac{1-\vartheta}{2}K_\mathrm{i}^h\left\|\boldsymbol{\eta}_\mathrm{d}^h\right\|^2 \\ &-\frac{\vartheta}{2}K_\mathrm{i}^h\left\|\boldsymbol{\eta}_\mathrm{d}^h\right\|\left(\left\|\boldsymbol{\eta}_\mathrm{d}^h\right\| - \frac{2\overline{\lambda}(\mathbf{P}_{\boldsymbol{\eta}_\mathrm{d}^h})}{\vartheta K_\mathrm{i}^h}\varphi\right),\end{aligned} \tag{75}$$

with $0 < \vartheta < 1$. Hence, if K_i^h is chosen such that

$$\left\|\boldsymbol{\eta}_\mathrm{d}^h\right\| \geq \frac{2\overline{\lambda}(\mathbf{P}_{\boldsymbol{\eta}_\mathrm{d}^h})}{\vartheta K_\mathrm{i}^h}\varphi_\infty,\ \varphi_\infty = \left\|\mathbf{K}^h\right\|\left\|\boldsymbol{\eta}_{\boldsymbol{\phi}}^h\right\|_\infty + \delta^h_{\max}, \tag{76}$$

then $\dot{V} \leq -\frac{1}{2}K_\mathrm{i}^h\left\|\boldsymbol{\eta}_\mathrm{d}^h\right\|^2$. By the virtue of [49, Theorem 4.18], $\boldsymbol{\eta}_\mathrm{d}^h$ is uniformly ultimately bounded with ultimate bound $\sigma = \sqrt{\frac{\overline{\lambda}(\mathbf{P}_{\boldsymbol{\eta}_\mathrm{d}^h})}{\underline{\lambda}(\mathbf{P}_{\boldsymbol{\eta}_\mathrm{d}^h})}}\frac{2\overline{\lambda}(\mathbf{P}_{\boldsymbol{\eta}_\mathrm{d}^h})}{\vartheta K_\mathrm{i}^h}\varphi_\infty$. In addition, there exists a closed set $\mathcal{C}_{\mathrm{d}\sigma}$ which is asymptotically stable and forward invariant[17]. Given that $\mathcal{C}_\mathrm{d} \subseteq \mathcal{C}_{\mathrm{d}\sigma}$ then following from Definition 1, $\mathcal{C}_\mathrm{d}$ is robustly stable, and thereby, from Definition 2, h_d is a RECBF. □

[16]Note that (71) allows to use the same theoretical tools as in the proof of Theorem 1 in Appendix D.

[17]Forward invariance and asymptotic stability follow from the uniform ultimate boundedness property of $\boldsymbol{\eta}_\mathrm{d}^h$.

F. Proof of Proposition 3

Proof. The superscript ^{i} is dropped for the sake of clarity. Substituting (44) in (17) yields to

$$\dot{\boldsymbol{\eta}}_{\mathrm{d}} = \check{\mathbf{F}}_{\boldsymbol{\eta}_{\mathrm{d}}}\boldsymbol{\eta}_{\mathrm{d}} - \mathbf{B}_{\boldsymbol{\eta}_{\mathrm{d}}}\mathbf{K}\boldsymbol{\eta}_{\boldsymbol{\phi}} + \mathbf{B}_{\boldsymbol{\eta}_{\mathrm{d}}}\delta(t).$$

Let us consider Lyapunov function V in (64) such that (65) holds. Following the same steps in Theorem 1 proof, $\dot{V}$ is bounded such that

$$\dot{V} \leq -\frac{1}{2}(1-\vartheta)\underline{\lambda}(\mathbf{K}_{\mathrm{i}})\left\|\boldsymbol{\eta}_{\mathrm{d}}\right\|^2 - \frac{\vartheta\underline{\lambda}(\mathbf{K}_{\mathrm{i}})}{2}\left\|\boldsymbol{\eta}_{\mathrm{d}}\right\|\left(\left\|\boldsymbol{\eta}_{\mathrm{d}}\right\| - \frac{2\overline{\lambda}(\mathbf{P}_{\boldsymbol{\eta}_{\mathrm{d}}})}{\vartheta\underline{\lambda}(\mathbf{K}_{\mathrm{i}})}\left(\left\|\mathbf{K}\right\|\left\|\boldsymbol{\eta}_{\boldsymbol{\phi}}\right\| + \left\|\delta(t)\right\|\right)\right).$$

If $\mathbf{K}_{\mathrm{i}}$ is chosen such that $\left\|\boldsymbol{\eta}_{\mathrm{d}}\right\| \geq \frac{2\overline{\lambda}(\mathbf{P}_{\boldsymbol{\eta}_{\mathrm{d}}})}{\vartheta\underline{\lambda}(\mathbf{K}_{\mathrm{i}})}\left(\left\|\mathbf{K}\right\|\left\|\boldsymbol{\eta}_{\boldsymbol{\phi}}\right\|_{\infty} + \delta_{\max}\right)$ then $\dot{V} \leq -\frac{1}{2}(1-\vartheta)\underline{\lambda}(\mathbf{K}_{\mathrm{i}})\left\|\boldsymbol{\eta}_{\mathrm{d}}\right\|^2$. From [49, Theorem 4.18], it follows that $\boldsymbol{\eta}_{\mathrm{d}}$ is uniformly ultimately bounded with ultimate bound $\varrho = \sqrt{\frac{\overline{\lambda}(\mathbf{P}_{\boldsymbol{\eta}_{\mathrm{d}}})}{\underline{\lambda}(\mathbf{P}_{\boldsymbol{\eta}_{\mathrm{d}}})}}\frac{2\overline{\lambda}(\mathbf{P}_{\boldsymbol{\eta}_{\mathrm{d}}})}{\vartheta\underline{\lambda}(\mathbf{K}_{\mathrm{i}})}\left(\left\|\mathbf{K}\right\|\left\|\boldsymbol{\eta}_{\boldsymbol{\phi}}\right\|_{\infty} + \delta_{\max}\right)$. Following the same steps in (68), $\boldsymbol{\eta}_{\mathrm{d}}$ is robustly practically stable w.r.t the residual set $\Omega_{\boldsymbol{\eta}_{\mathrm{d}}} = \{\boldsymbol{\eta}_{\mathrm{d}} \in H : \left\|\boldsymbol{\eta}_{\mathrm{d}}\right\| \leq \varrho\}$. □

REFERENCES

[1] C. Samson, M. Le Borgne, and B. Éspiau, *Robot control: the task function approach*. Oxford engineering science series, Clarendon Press, 1991.

[2] A. Ramadorai, T.-J. Tara, A. Bejczy, and N. Xi, "Task-driven control of multi-arm systems," *IEEE Transactions on Control Systems Technology*, vol. 2, no. 3, pp. 198–206, 1994.

[3] A. D. Ames, X. Xu, J. W. Grizzle, and P. Tabuada, "Control barrier function based quadratic programs for safety critical systems," *IEEE Transactions on Automatic Control*, vol. 62, no. 8, pp. 3861–3876, 2017.

[4] W. Shaw Cortez, D. Oetomo, C. Manzie, and P. Choong, "Control barrier functions for mechanical systems: Theory and application to robotic grasping," *IEEE Transactions on Control Systems Technology*, vol. 29, no. 2, pp. 530–545, 2021.

[5] M. Djeha, A. Tanguy, and A. Kheddar, "Adaptive-gains enforcing constraints in closed-loop qp control," *IEEE Robotics and Automation Letters*, vol. 5, no. 4, pp. 6504–6511, 2020.

[6] A. Escande, N. Mansard, and P.-B. Wieber, "Hierarchical quadratic programming: Fast online humanoid-robot motion generation," *The International Journal of Robotics Research*, vol. 33, no. 7, pp. 1006–1028, 2014.

[7] J. Salini, V. Padois, and P. Bidaud, "Synthesis of complex humanoid whole-body behavior: A focus on sequencing and tasks transitions," in *IEEE International Conference on Robotics and Automation*, pp. 1283–1290, 2011.

[8] A. Herzog, N. Rotella, S. Mason, F. Grimminger, S. Schaal, and L. Righetti, "Momentum control with hierarchical inverse dynamics on a torque-controlled humanoid," *Autonomous Robots*, vol. 40, no. 3, pp. 473–491, 2016.

[9] S. Kuindersma, R. Deits, M. Fallon, A. Valenzuela, H. Dai, F. Permenter, T. Koolen, P. Marion, and R. Tedrake, "Optimization-based locomotion planning, estimation, and control design for the atlas humanoid robot," *Autonomous Robots*, vol. 40, no. 3, pp. 429–455, 2016.

[10] G. Nava, Q. Sablé, M. Tognon, D. Pucci, and A. Franchi, "Direct force feedback control and online multi-task optimization for aerial manipulators," *IEEE Robotics and Automation Letters*, vol. 5, no. 2, pp. 331–338, 2020.

[11] K. A. Hamed, J. Kim, and A. Pandala, "Quadrupedal locomotion via event-based predictive control and qp-based virtual constraints," *IEEE Robotics and Automation Letters*, vol. 5, no. 3, pp. 4463–4470, 2020.

[12] J. Englsberger, C. Ott, and A. Albu-Schäffer, "Three-dimensional bipedal walking control based on divergent component of motion," *IEEE Transactions on Robotics*, vol. 31, no. 2, pp. 355–368, 2015.

[13] V. Klemm, A. Morra, L. Gulich, D. Mannhart, D. Rohr, M. Kamel, Y. de Viragh, and R. Siegwart, "Lqr-assisted whole-body control of a wheeled bipedal robot with kinematic loops," *IEEE Robotics and Automation Letters*, vol. 5, no. 2, pp. 3745–3752, 2020.

[14] E. A. Basso and K. Y. Pettersen, "Task-priority control of redundant robotic systems using control lyapunov and control barrier function based quadratic programs," *IFAC-PapersOnLine*, vol. 53, no. 2, pp. 9037–9044, 2020. 21st IFAC World Congress.

[15] S. Feng, E. Whitman, X. Xinjilefu, and C. G. Atkeson, "Optimization-based full body control for the DARPA robotics challenge," *Journal of Field Robotics*, vol. 32, no. 2, pp. 293–312, 2015.

[16] M. Johnson, B. Shrewsbury, S. Bertrand, T. Wu, D. Duran, M. Floyd, P. Abeles, D. Stephen, N. Mertins, A. Lesman, J. Carff, W. Rifenburgh, P. Kaveti, W. Straatman, J. Smith, M. Griffioen, B. Layton, T. de Boer, T. Koolen, P. Neuhaus, and J. Pratt, "Team ihmc's lessons learned from the darpa robotics challenge trials," *Journal of Field Robotics*, vol. 32, no. 2, pp. 192–208, 2015.

[17] M. DeDonato, F. Polido, K. Knoedler, B. P. W. Babu, N. Banerjee, C. P. Bove, X. Cui, R. Du, P. Franklin, J. P. Graff, P. He, A. Jaeger, L. Li, D. Berenson, M. A. Gennert, S. Feng, C. Liu, X. Xinjilefu, J. Kim, C. G. Atkeson, X. Long, and T. Padır, "Team wpi-cmu: Achieving reliable humanoid behavior in the darpa robotics challenge," *Journal of Field Robotics*, vol. 34, no. 2, pp. 381–399, 2017.

[18] T. Koolen, S. Bertrand, G. Thomas, T. De Boer, T. Wu, J. Smith, J. Englsberger, and J. Pratt, "Design of a momentum-based control framework and application to the humanoid robot atlas," *International Journal of Humanoid Robotics*, vol. 13, no. 01, p. 1650007, 2016.

[19] J. Englsberger, A. Werner, C. Ott, B. Henze, M. A. Roa, G. Garofalo, R. Burger, A. Beyer, O. Eiberger, K. Schmid, *et al.*, "Overview of the torque-controlled humanoid robot toro," in *IEEE-RAS International Conference on Humanoid Robots*, pp. 916–923, Nov 2014.

[20] M. A. Hopkins, D. W. Hong, and A. Leonessa, "Compliant locomotion using whole-body control and divergent component of motion tracking," in *2015 IEEE International Conference on Robotics and Automation*, pp. 5726–5733, May 2015.

[21] J. Lee, J. Ahn, D. Kim, S. H. Bang, and L. Sentis, "Online gain adaptation of whole-body control for legged robots with unknown disturbances," *Frontiers in Robotics and AI*, vol. 8, 2022.

[22] R. Cisneros, M. Benallegue, A. Benallegue, M. Morisawa, H. Audren, P. Gergondet, A. Escande, A. Kheddar, and F. Kanehiro, "Robust humanoid control using a qp solver with integral gains," in *IEEE/RSJ International Conference on Intelligent Robots and Systems*, pp. 7472–7479, Oct 2018.

[23] A. Singletary, S. Kolathaya, and A. D. Ames, "Safety-critical kinematic control of robotic systems," *IEEE Control Systems Letters*, vol. 6, pp. 139–144, 2022.

[24] T. G. Molnar, R. K. Cosner, A. W. Singletary, W. Ubellacker, and A. D. Ames, "Model-free safety-critical control for robotic systems," *IEEE Robotics and Automation Letters*, vol. 7, no. 2, pp. 944–951, 2022.

[25] C. Yang, K. Yuan, W. Merkt, T. Komura, S. Vijayakumar, and Z. Li, "Learning whole-body motor skills for humanoids," in *IEEE-RAS International Conference on Humanoid Robots*, pp. 270–276, 2018.

[26] M. Iskandar, C. Ott, O. Eiberger, M. Keppler, A. Albu-Schäeffer, and A. Dietrich, "Joint-level control of the dlr lightweight robot sara," in *IEEE/RSJ International Conference on Intelligent Robots and Systems*, 10 2020.

[27] T. Pang and R. Tedrake, "Easing reliance on collision-free planning with contact-aware control," in *International Conference on Robotics and Automation*, pp. 8375–8381, 2022.

[28] J. Garcia, A. Robertsson, J. Ortega, and R. Johansson, "Sensor fusion of force and acceleration for robot force control," in *IEEE/RSJ International Conference on Intelligent Robots and Systems*, vol. 3, pp. 3009–3014 vol.3, 2004.

[29] R. Rossi, L. Bascetta, and P. Rocco, "Implicit force control for an industrial robot with flexible joints and flexible links," in *IEEE/RSJ International Conference on Intelligent Robots and Systems*, pp. 4742–4749, 2014.

[30] A. M. Zanchettin and P. Rocco, "Motion planning for robotic manipulators using robust constrained control," *Control Engineering Practice*, vol. 59, pp. 127–136, 2017.

[31] M. P. Polverini, D. Nicolis, A. M. Zanchettin, and P. Rocco, "Implicit robot force control based on set invariance," *IEEE Robotics and Automation Letters*, vol. 2, no. 3, pp. 1288–1295, 2017.

[32] F. Suárez-Ruiz, X. Zhou, and Q.-C. Pham, "Can robots assemble an ikea chair?," *Science Robotics*, vol. 3, no. 17, 2018.

[33] J. Lim and J.-H. Oh, "Backward ladder climbing locomotion of humanoid robot with gain overriding method on position control," *Journal of Field Robotics*, vol. 33, no. 5, pp. 687–705, 2016.

[34] A. Singletary, W. Guffey, T. G. Molnar, R. Sinnet, and A. D. Ames, "Safety-critical manipulation for collision-free food preparation," *IEEE Robotics and Automation Letters*, vol. 7, no. 4, pp. 10954–10961, 2022.

[35] Y. Shi, X. He, W. Zou, B. Yu, L. Yuan, M. Li, G. Pan, and K. Ba, "Multi-objective optimal torque control with simultaneous motion and force tracking for hydraulic quadruped robots," *Machines*, vol. 10, no. 3, 2022.
[36] K. Bouyarmane and A. Kheddar, "On weight-prioritized multitask control of humanoid robots," *IEEE Transactions on Automatic Control*, vol. 63, pp. 1632–1647, June 2018.
[37] M. P. Polverini, A. M. Zanchettin, F. Incocciati, and P. Rocco, "Robust constraint-based robot control for bimanual cap rotation," in *IEEE/RSJ International Conference on Intelligent Robots and Systems*, pp. 4785–4790, 2017.
[38] D. Kim, S. J. Jorgensen, P. Stone, and L. Sentis, "Dynamic behaviors on the nao robot with closed-loop whole body operational space control," in *IEEE-RAS International Conference on Humanoid Robots*, pp. 1121–1128, 2016.
[39] K. Pfeiffer, A. Escande, P. Gergondet, and A. Kheddar, "The hierarchical newton's method for numerically stable prioritized dynamic control," *IEEE Transactions on Control Systems Technology*, vol. 31, no. 4, pp. 1622–1635, 2023.
[40] S. Kolathaya and A. D. Ames, "Input-to-state safety with control barrier functions," *IEEE Control Systems Letters*, vol. 3, no. 1, pp. 108–113, 2019.
[41] K. Bouyarmane and A. Kheddar, "Using a multi-objective controller to synthesize simulated humanoid robot motion with changing contact configurations," in *IEEE/RSJ International Conference on Intelligent Robots and Systems*, pp. 4414–4419, Sep. 2011.
[42] B. Siciliano, L. Sciavicco, L. Villani, and G. Oriolo, *Robotics: modelling, planning and control*. Springer Science and Business Media, 2010.
[43] E. D. Sontag, *Input to State Stability: Basic Concepts and Results*, pp. 163–220. Berlin, Heidelberg: Springer Berlin Heidelberg, 2008.
[44] S. N. Dashkovskiy, D. V. Efimov, and E. D. Sontag, "Input to state stability and allied system properties," *Automation and Remote Control*, vol. 72, p. 1579, Aug 2011.
[45] S. Moberg, J. Ohr, and S. Gunnarsson, "A benchmark problem for robust feedback control of a flexible manipulator," *IEEE Transactions on Control Systems Technology*, vol. 17, no. 6, pp. 1398–1405, 2009.
[46] F. Blanchini, "Set invariance in control," *Automatica*, vol. 35, no. 11, pp. 1747–1767, 1999.
[47] X. Xu, P. Tabuada, J. W. Grizzle, and A. D. Ames, "Robustness of control barrier functions for safety critical control," *IFAC-PapersOnLine*, vol. 48, no. 27, pp. 54–61, 2015. Analysis and Design of Hybrid Systems ADHS.
[48] A. D. Ames, S. Coogan, M. Egerstedt, G. Notomista, K. Sreenath, and P. Tabuada, "Control barrier functions: Theory and applications," in *European Control Conference*, pp. 3420–3431, 2019.
[49] H. K. Khalil, *Nonlinear systems; 3rd ed.* Upper Saddle River, NJ: Prentice-Hall, 2002.
[50] J. J. Quiroz-Omaña and B. V. Adorno, "Whole-body control with (self) collision avoidance using vector field inequalities," *IEEE Robotics and Automation Letters*, vol. 4, no. 4, pp. 4048–4053, 2019.
[51] W. Decré, R. Smits, H. Bruyninckx, and J. De Schutter, "Extending itasc to support inequality constraints and non-instantaneous task specification," in *IEEE International Conference on Robotics and Automation*, pp. 964–971, 2009.
[52] S. Rubrecht, V. Padois, P. Bidaud, and M. De Broissia, "Constraints compliant control: constraints compatibility and the displaced configuration approach," in *IEEE/RSJ International Conference on Intelligent Robots and Systems*, pp. 677–684, 2010.
[53] A. del Prete, "Joint position and velocity bounds in discrete-time acceleration/torque control of robot manipulators," *IEEE Robotics and Automation Letters*, vol. 3, pp. 281–288, Jan 2018.
[54] H. Audren and A. Kheddar, "3-d robust stability polyhedron in multicontact," *IEEE Transactions on Robotics*, vol. 34, no. 2, pp. 388–403, 2018.
[55] K. Bouyarmane, K. Chappellet, J. Vaillant, and A. Kheddar, "Quadratic programming for multirobot and task-space force control," *IEEE Transactions on Robotics*, vol. 35, pp. 64–77, Feb 2019.
[56] R. A. Freeman and P. V. Kokotovic, "Robust control lyapunov functions: the measurement feedback case," in *Proceedings of 33rd IEEE Conference on Decision and Control*, vol. 4, pp. 3533–3538 vol.4, 1994.
[57] R. A. Freeman and P. V. Kototovic, *Robust Nonlinear Control Design: State-Space and Lyapunov Techniques*. USA: Birkhauser Boston Inc., 1996.
[58] W. J. Rugh, *Linear System Theory, Second Edition*. Prentice Hall, 2 ed., 1996.
[59] G. Strang, *Linear algebra and its applications*. Harcourt, Brace, Jovanovich, Publishers, 3rd ed., 1988.
[60] N. Piskunov, *Differential and Integral Calculus*. Mir, 1st ed., 1969.
[61] G. Golub and C. Van Loan, *Matrix Computations*. The Johns Hopkins University Press, 4th ed., 2013.

Mohamed Djeha received both the B.S. and M.S. degree in 2017 from Ecole Militaire Polytechnique (EMP), Algiers in Systems Control. He then received the Ph.D. degree in robotics from the University of Montpellier in September 2022.

His MS research was focused on exploiting electrophysiological signals to control robotics systems using machine learning and data fusion techniques. His Ph.D. research has been conducted at CNRS-University of Montpellier LIRMM in Montpellier on multi-objective and optimization-based control for redundant robotic manipulators and humanoids. Currently, he is a researcher at the Laboratory of Complex Systems Control and Simulators at EMP.

Pierre Gergondet received the M.S. degree in 2010 from École Centrale de Paris with a speciality in embedded systems. He then received the Ph.D. degree in robotics from the University of Montpellier in 2014.

His Ph.D. research was conducted on controlling humanoid robot using brain-computer interfaces at the CNRS-AIST Joint Robotics Laboratory (JRL), IRL 3218 in Tsukuba Japan. He continued to work in JRL as a CNRS Research Engineer leading the software developments of the multi-contact real time framework: mc_rtc. Between 2019 and 2022, he joined the Beijing Advanced Innovation Center for Intelligent Robots and Systems (BAICIRS) at the Beijing Institute of Technology (BIT) as a special associate researcher, he has since resumed his position at JRL. His current research interests include humanoid robots, control software for robotics and robotics applications.

Abderrahmane Kheddar (F'22, SM'12, M'08) received the B.S. in Computer Science degree from the Institut National d'Informatique (ESI), Algiers, Algeria in 1990, and the M.Sc. and Ph.D. degree in robotics, both from Pierre et Marie Curie University, Sorbonne University, Paris, France 1993 and 1997, respectively.

He is presently Directeur de Recherche at CNRS at the CNRS-AIST Joint Robotic Laboratory (JRL), IRL, Tsukuba, Japan (that he created in 2008, Director from 2008 to 2018). He also created and led the Interactive Digital Humans (IDH) team at CNRS-University of Montpellier LIRMM (from 2010 to 2020), France. His research interests include haptics, humanoids and thought-based control using brain machine interfaces. He is a founding member of the IEEE/RAS chapter on haptics, the co-chair and founding member of the IEEE/RAS Technical committee on model-based optimization, he is a member of the steering committee of the IEEE Brain Initiative, Editor of the IEEE Robotics and Automation Letters, Founding member and Deputy Editor-in-Chief of Cyborg and Bionics System (a Science partner journal). He was Editor of the IEEE Transactions on Robotics (2013-2018) and within the editorial board of other robotics journals; he is a founding member of the IEEE Transactions on Haptics and served in its editorial board during three years (2007-2010). He is an IEEE Fellow, AAIA Fellow and titular full member of the National Academy of Technology of France and knight of the national order of merits of France.